Flow Turbulence Combust (2016) 96:1053–1081
DOI 10.1007/s10494-016-9724-7

Flame Structure and Propagation in Turbulent Flame-Droplet Interaction: A Direct Numerical Simulation Analysis

Daniel H. Wacks[1] · **Nilanjan Chakraborty**[2]

Received: 15 October 2015 / Accepted: 2 March 2016 / Published online: 30 March 2016

Abstract Three-dimensional Direct Numerical Simulations (DNS) in canonical configuration have been employed to study the combustion of mono-disperse droplet-mist under turbulent flow conditions. A parametric study has been performed for a range of values of droplet equivalence ratio ϕ_d, droplet diameter a_d and root-mean-square value of turbulent velocity u'. The fuel is supplied entirely in liquid phase such that the evaporation of the droplets gives rise to gaseous fuel which then facilitates flame propagation into the droplet-mist. The combustion process in gaseous phase takes place predominantly in fuel-lean mode even for $\phi_d > 1$. The probability of finding fuel-lean mixture increases with increasing initial droplet diameter because of slower evaporation of larger droplets. The chemical reaction is found to take place under both premixed and non-premixed modes of combustion: the premixed mode ocurring mainly under fuel-lean conditions and the non-premixed mode under stoichiometric or fuel-rich conditions. The prevalence of premixed combustion was seen to decrease with increasing droplet size. Furthermore, droplet-fuelled turbulent flames have been found to be thicker than the corresponding turbulent stoichiometric premixed flames and this thickening increases with increasing droplet diameter. The flame thickening in droplet cases has been explained in terms of normal strain rate induced by fluid motion and due to flame normal propagation arising from different components of displacement speed. The statistical behaviours of the effective normal strain rate and flame stretching have been analysed in detail and detailed physical explanations have been provided for the observed behaviour. It has been found that the droplet cases show higher probability of

✉ Daniel H. Wacks
daniel.h.wacks@durham.ac.uk

Nilanjan Chakraborty
nilanjan.chakraborty@ncl.ac.uk

[1] School of Engineering and Computing Sciences, Durham University, Lower Mountjoy, South Road, Durham DH1 3LE, UK

[2] School of Mechanical and Systems Engineering, Newcastle University, Claremont Road, Newcastle-Upon-Tyne, NE1 7RU, UK

finding positive effective normal strain rate (i.e. combined contribution of fluid motion and flame propagation), and negative values of stretch rate than in the stoichiometric premixed flame under similar flow conditions, which are responsible for higher flame thickness and smaller flame area generation in droplet cases.

Keywords Direct numerical simulation · Turbulent combustion · Droplet diameter · Droplet equivalence ratio · Turbulence intensity

1 Introduction

Flame propagation into droplet-laden mixtures plays a pivotal role in several engineering applications ranging from Internal Combustion (IC) engines (e.g. Direct Injection and Compression Ignition engines) [1, 2] to aero gas turbines [2, 3], as well as in hazard prediction and control [4]. In spite of its extensive applicability, this topic has received relatively limited attention. The classic experimental work by Burgoyne and Cohen [5] indicated that the droplet diameter of the resident liquid droplets and their concentration can have significant effects on the subsequent flame propagation and burning rate. Likewise, Faeth and his co-workers [6, 7] indicated in a number of experimental investigations that evaporation characteristics of the droplets can also contribute to the subsequent flame propagation behaviour. It was experimentally demonstrated by Ballal and Lefebvre [8] that the flame speed for droplets small enough to evaporate completely before reaching the flame front was similar to that of a purely gaseous mixture and that the flame speed decreases with increasing initial droplet diameter. Ballal and Lefebvre [8] experimentally observed that there exists an optimal initial droplet diameter for a given fuel and overall equivalence ratio, $\phi_{ov} = \phi_g + \phi_d$ (where ϕ_g is the contribution arising due to gaseous fuel and ϕ_d the contribution arising due to liquid fuel), for which the laminar flame propagation was enhanced compared to that of a purely gaseous fuel. This enhanced flame speed was observed experimentally for both lean ($\phi_{ov} < 1.0$) and rich ($\phi_{ov} > 1.0$) overall equivalence ratios [9]. For an overall rich flame, it was suggested that the flame speed enhancement was due to the incomplete evaporation of large droplets on the unburned gas side which led to a local gaseous equivalence ratio close to unity (i.e. close to stoichiometry) in the region of the flame front [10–12]. Moreover, the inertia of fuel droplets causes them to lag behind the accelerating gas ahead of the flame. This, in turn, may lead to enrichment of fuel vapour, which gives rise to augmented (reduced) burning rate for lean (rich) droplet-laden mixtures under quiescent conditions, although this effect disappears at higher values of turbulence intensity [13]. The equivalence ratio of fuel in the gaseous mixture following the evaporation process was also shown to have significant effects on flame propagation [13], but these effects also weaken with increasing level of turbulent velocity fluctuation [13].

Neophytou and Mastorakos [14] numerically analysed the effects of volatility, droplet diameter and droplet equivalence ratio on burning velocity in one-dimensional flames where fuel is supplied in the form of mono-disperse droplets based on detailed chemistry n-heptane and n-decane laminar flame simulations. Two-dimensional unsteady laminar counter-flow simulations have also been used by Nakamura et al. [15] and Watanabe et al. [16, 17] to analyse the effects of equivalence ratio, droplet diameter and droplet group number on n-decane spray flame structure. Fujita et al. [18] analysed the same effects using two-dimensional jet flame simulations. Neophytou and Mastorakos [14] indicated that 'small' droplets with overall equivalence ratio ϕ_{ov} either less than or equal to 1.0 (i.e. $\phi_{ov} \leq 1.0$) and 'large'

droplets with overall equivalence ratio greater than one (i.e. $\phi_{ov} > 1.0$) yield high values of burning velocity and chemical reaction rate. Furthermore, it has been demonstrated by Neophytou and Mastorakos [14] that combustion can be sustained even for ϕ_{ov} values which are greater than the rich-flammability limit for gaseous fuel-air mixture. This behaviour arises due to incomplete evaporation of the droplets, which leads to a gaseous equivalence ratio value much lower than the overall equivalence ratio. Recently, Wacks et al. [19] extended the analysis by Neophytou and Mastorakos [14] for turbulent flames by carrying out three-dimensional compressible Direct Numerical Simulations (DNS) of freely propagating turbulent flame propagation into droplet-laden mixtures. Wacks et al. [19] used the DNS data to analyse the effects of initial droplet diameter, a_d, droplet equivalence ratio, ϕ_d, and turbulence intensity, u', on the flame structure and the statistical behaviour of flame propagation into droplet-laden mixtures. It has been found based on numerical results that the resulting spray flame structure exhibits a considerable extent of premixed combustion in addition to an expected diffusion mode of burning [15–19]. The extent of premixed mode of combustion has been found to increase with decreasing droplet diameter [15–19]. Moreover, the burned gas temperature can be different from a gaseous diffusion flame due to the combined effects of latent heat of evaporation and premixed combustion [15–19]. Nakamura et al. [15] also argued that the group combustion number, which is defined based on a homogenous field of unburned droplets and air mixture, is not sufficient to characterize the combustion process in spray flames due to the premixed-like combustion. Wacks et al. [19] demonstrated predominantly fuel-lean mode of combustion even for $\phi_d > 1$, which has been shown to significantly affect the flame surface area generation, local flame propagation and flame thickness. From the foregoing it is evident that flame propagation in turbulent droplet-laden mixtures is a complex process where evaporative heat and mass transfer, fluid dynamics, combustion and thermo-chemistry are simultaneously at play. A robust physical understanding of flame propagation in droplet-laden mixtures and its modelling will play a key role in the design and development of modern reliable energy-efficient and environment-friendly IC engines and gas turbine combustors.

The current analysis further extends that of Neophytou and Mastorakos [14] and Wacks et al. [19] for turbulent flames by carrying out three-dimensional compressible DNS of freely propagating turbulent flame propagation into droplet-laden mixtures. In recent times, both single-step [18–29] or detailed [30, 31] chemistry based DNS analyses have contributed significantly to the physical understanding and modelling of the combustion of turbulent droplet-laden mixtures. In the aforementioned DNS studies, the gaseous phase is treated in a typical Eulerian fashion and the droplets are considered as sub-grid particles which are tracked in a Lagrangian manner. In this numerical framework, appropriate source terms involving suitable relaxation time-scales have been used in the gaseous phase for the mass, momentum and energy conservations in order to account for the contributions arising due to droplet evaporation. The same treatment of droplets as sub-grid particles will also be adopted here to analyse the statistical behaviour of flame-droplet interaction. Here the DNS data has been used to analyse the effects of initial droplet diameter, a_d, droplet equivalence ratio, ϕ_d, and turbulence intensity, u', on the reaction zone structure and flame stretching in turbulent spray flames. In this respect, the main objectives of the present study are:

1. To demonstrate and explain the effects of a_d, ϕ_d and u' on the reaction zone structure when fuel is supplied in the form of monodisperse droplets on the unburned gas side of the flame.
2. To investigate the effects of a_d, ϕ_d and u' on the mechanisms governing flame thickness in spray flames.

The remainder of the paper takes the following form. The next section discusses the necessary mathematical background related to the current study. A brief discussion of the numerical implementation used in the present study is then presented. Following this, the results are presented and subsequently discussed. Finally the main findings are summarised and conclusions are drawn.

2 Mathematical Background

In the current analysis, a single-step irreversible Arrhenius-type chemical mechanism has been used for the purpose of carrying out the present extensive parametric analysis at a modest computational cost:

$$\text{Fuel} + \text{ s } \cdot \text{ Oxidiser} \rightarrow (1+\text{s}) \cdot \text{ Products} \tag{1}$$

where s is the oxidiser-fuel ratio by mass (i.e. the mass of oxygen consumed per unit mass of fuel). The fuel reaction rate $\dot{\omega}_{\text{F}}$ is expressed as:

$$\dot{\omega}_{\text{F}} = -\rho \text{B}^{*} \text{Y}_{\text{F}} \text{Y}_{\text{O}} \exp\left(-\frac{\beta\,(1-\text{T})}{1-\alpha\,(1-\text{T})}\right) \tag{2}$$

where ρ is the gas density and Y_{F} and Y_{O} are the fuel and oxygen mass fractions respectively, T, the non-dimensional temperature, β, the Zeldovich number, α, a heat release parameter, and B^{*}, the normalised pre-exponential factor, are given by following expressions:

$$\text{T} = \left(\frac{\hat{\text{T}} - \text{T}_0}{\text{T}_{\text{ad}(\phi_{\text{g}}=1)} - \text{T}_0}\right); \beta = \frac{\text{E}_{\text{ac}}\left(\text{T}_{\text{ad}(\phi_{\text{g}}=1)} - \text{T}_0\right)}{\text{R}_0 \text{T}^2_{\text{ad}(\phi_{\text{g}}=1)}}; \alpha = \frac{\tau}{1+\tau} = \frac{\left(\text{T}_{\text{ad}(\phi_{\text{g}}=1)} - \text{T}_0\right)}{\text{T}_{\text{ad}(\phi_{\text{g}}=1)}} \text{ and } \text{B}^{*} = \text{ Bexp}\left(-\frac{\beta}{\alpha}\right) \tag{3}$$

where $\hat{\text{T}}$ is the instantaneous dimensional temperature, T_0 is the unburned gas temperature, $\text{T}_{\text{ad}(\phi_{\text{g}}=1)}$ is the adiabatic flame temperature for the stoichiometric mixture, E_{ac} is the activation energy, R_0 is the universal gas constant, B is the pre-exponential factor and $\tau = \left(\text{T}_{\text{ad}(\phi_{\text{g}}=1)} - \text{T}_0\right)/\text{T}_0$ is a heat release parameter. Here, the activation energy, E_{ac}, and the heat of combustion are taken to be functions of the gaseous equivalence ratio, ϕ_{g}, following the suggestion of Tarrazo et al. [32], which correctly predicts the equivalence ratio ϕ_{g} dependence of the unstrained laminar burning velocity $\text{S}_{\text{b}(\phi_{\text{g}})}$ in hydrocarbon-air flames, especially for fuel-rich mixtures. According to Tarrazo et al. [32], the Zel'dovich number, β, is given by $\beta = 6f\left(\phi_{\text{g}}\right)$ where:

$$\text{f}\left(\phi_{\text{g}}\right) = \begin{cases} 1.0 + 8.250\left(\phi_{\text{g}} - 1.00\right)^2 & , \phi_{\text{g}} \leq 0.64 \\ 1.0 & , 0.64 < \phi_{\text{g}} < 1.07 \\ 1.0 + 1.443\left(\phi_{\text{g}} - 1.07\right)^2 & , \phi_{\text{g}} \geq 1.07 \end{cases} \tag{4}$$

Furthermore, the heat release per unit mass of $\text{fuel} \text{H}_{\phi_{\text{g}}} = \left[\left(\text{T}_{\text{ad}(\phi_{\text{g}})} - \text{T}_0\right)\text{C}_{\text{P}}\right] / \left[\text{Y}_{\text{F0}(\phi_{\text{g}})} - \text{Y}_{\text{Fb}(\phi_{\text{g}})}\right]$ is given by $\text{H}_{\phi_{\text{g}}}/\text{H}_{\phi\text{g}} = 1 = 1$ for $\phi_{\text{g}} \leq 1$ and $\text{H}_{\phi_{\text{g}}}/\text{H}_{\phi_{\text{g}}} = 1 = 1 - \alpha_{\text{H}}\left(\phi_{\text{g}} - 1\right)$ for $\phi_{\text{g}} > 1$ [32], where $\alpha_{\text{H}} = 0.18$ and $\text{Y}_{\text{F0}(\phi_{\text{g}})}$ and $\text{Y}_{\text{Fb}(\phi_{\text{g}})}$ are the fuel mass fraction in the unburned and burned gases respectively for a premixed flame of equivalence ratio ϕ_{g}. The Lewis numbers of all species are taken to be equal to unity and all species in gaseous phase are taken to be perfect gases. Standard values have been taken for the ratio of specific heats ($\gamma = \text{C}^{\text{g}}_{\text{P}}/\text{C}^{\text{g}}_{\text{V}} = 1.4$, where

C_P^g and C_V^g are the gaseous specific heats at constant pressure and volume respectively) and Prandtl number ($Pr = \mu C_P^g / \lambda = 0.7$ where μ, is the dynamic viscosity and λ is the thermal conductivity of the gaseous phase).

The droplet transport equations considered by Reveillon and Vervisch [21] have been used for the purpose of this analysis. The quantities transported for each droplet are the position, $\vec{x}_d$, velocity, $\vec{u}_d$, diameter, a_d and temperature, T_d, and the transport equations for these quantities are given by:

$$\frac{d\vec{x}_d}{dt} = \vec{u}_d \tag{5}$$

$$\frac{d\vec{u}_d}{dt} = \frac{\vec{u}\,(\vec{x}_d, t) - \vec{u}_d}{\tau_d^p} \tag{6}$$

$$\frac{da_d^2}{dt} = -\frac{a_d^2}{\tau_d^u} \tag{7}$$

$$\frac{dT_d}{dt} = -\frac{\hat{T}\,(\vec{x}_d, t) - T_d - B_d L_v / C_P^g}{\tau_d^T} \tag{8}$$

where L_v is the latent heat of vaporization, and τ_d^p, τ_d^u and τ_d^T are the relaxation/decay timescales for droplet velocity, diameter and temperature respectively, which are defined as:

$$\tau_d^p = \frac{\rho_d a_d^2}{18 C_u \mu};\ \tau_d^u = \frac{\rho_d a_d^2}{4\mu}\frac{Sc}{Sh_c}\frac{1}{\ln(1+B_d)} \text{ and } \tau_d^T = \frac{\rho_d a_d^2}{6\mu}\frac{Pr}{Nu_c}\frac{B_d}{\ln?(1+B_d)}\frac{C_p^L}{C_p^g} \tag{9}$$

where ρ_d is the droplet density, C_p^L is the specific heat for the liquid phase, C_u is the corrected drag coefficient and is given by:

$$C_u = 1 + \frac{1}{6} Re_d^{2/3} \tag{10}$$

Furthermore, Re_d is the droplet Reynolds number, Sc is the Schmidt number, B_d is the Spalding mass transfer number, Sh_c is the corrected Sherwood number and Nu_c is the corrected Nusselt number, which are defined as [21, 33]:

$$Re_d = \frac{\rho\,|\vec{u}\,(\vec{x}_d, t) - \vec{u}_d|\,a_d}{\mu} \tag{11}$$

$$B_d = \frac{Y_F^s - Y_F(\vec{x}_d, t)}{1 - Y_F^s} \tag{12}$$

$$Sh_c = Nu_c = 2 + \frac{0.555 Re_d Sc}{\left(1.232 + Re_d Sc^{4/3}\right)^{1/2}} \tag{13}$$

where Y_F^s is the value of Y_F at the surface of the droplet. Equations 11–13 implicitly invoke the unity Lewis number assumption. The Clausius–Clapeyron relation for the partial pressure of the fuel vapour at the droplet surface, p_F^s, is used to evaluate the Spalding number B_d, which leads to:

$$p_F^s = p_{ref} \exp\left(\frac{L_v}{R_0}\left[\frac{1}{T_{ref}^s} - \frac{1}{T_d^s}\right]\right);\ Y_F^s = \left(1 + \frac{W_O}{W_F}\left[\frac{p(\vec{x}_d, t)}{p_F^s} - 1\right]\right)^1 \tag{14}$$

where T^s_{ref} is the boiling point of the fuel at pressure p_{ref}, R_0 is the universal gas constant, T^s_d is assumed to be T_d, and W_O and W_F are the molecular weights of oxidiser and fuel respectively.

The droplets are coupled to the gaseous phase via additional source terms in the gaseous transport equations, which may be generically written as [18–31]:

$$\frac{\partial \rho\psi}{\partial t}+\frac{\partial \rho u_j \psi}{\partial x_j}=\frac{\partial}{\partial x_j}\left(\Gamma_\psi \frac{\partial \psi_1}{\partial x_j}\right)+\dot{\omega}_\psi+\dot{S}_g+\dot{S}_\psi \tag{15i}$$

where $\psi=\{1,u_j,e,Y_F,Y_O\}$ for the conservation equations of mass, momentum, energy and mass fractions respectively. In Eq. 15i, $\psi_1=\{1,u_j,\hat{T},Y_F,Y_O\}$ for $\psi=\{1,u_j,e,Y_F,Y_O\}$ and $\Gamma_\psi=\mu/\sigma_\psi$ and λ for $\psi=\{u_j, Y_F, Y_O$ and $\psi=e$ respectively, with u_j and e being the velocity in the j^{th} direction and specific stagnation internal energy, respectively. The $\dot{\omega}_\psi$ term arises due to chemical reaction rate and $\dot{S}_g$ and $\dot{S}_\psi$ are the appropriate source terms in the gaseous phase and due to droplet evaporation, respectively. The droplet source term $\dot{S}_\psi$ is tri-linearly interpolated from the droplet's sub-grid position, $\vec{x}_d$, to the eight surrounding nodes. This approach is preferred, rather than each droplet contributing only to the nearest node, which would render the droplet's contribution discontinuous in time as it approached a different node. Furthermore, the method used here is second order, as opposed to assigning the contribution to the nearest node, which is only first order. The droplet source term for any variable ψ may be expressed as:

$$\dot{S}_\psi=-\frac{1}{V}\sum\nolimits_d \frac{dm_d\psi_d}{dt} \tag{15ii}$$

where V is the cell volume, $m_d=\rho_d\frac{1}{6}\pi a_d^3$ is the droplet mass and the summation is carried out over all droplets in the vicinity of each node. As noted with regard to Eq. 15i, the variable ψ is identified as $\psi=\{1,u_j,e,Y_F,Y_O\}$, however, since within the droplets $Y_F=1.0$, the source term for both the continuity equation and the fuel mass fraction equation are identical. The variable, σ_ψ, is an appropriate Schmidt number corresponding to ψ.

Droplet evaporation leads to mixture inhomogeneities, which can be characterized by the mixture fraction, which is defined as:

$$\xi=\frac{\left(Y_F-Y_O/s+Y_{O\infty}/s\right)}{\left(Y_{F\infty}+Y_{O\infty}/s\right)} \tag{16}$$

where $Y_{F\infty}=1.0$ is the fuel mass fraction in the pure fuel stream and $Y_{O\infty}=0.233$ is the oxidizer mass fraction in air. The hydrocarbon fuel used in this DNS analysis is n-heptane, C_7H_{16}, for which $s=3.52$ and the stoichiometric fuel mass fraction and mixture fraction values are given by: $Y_{Fst}=\xi_{st}=0.0621$. One can furthermore define a reaction progress variable,c, based on a species mass fraction and the mixture fraction such that c rises monotonically from zero in the unburnt reactants to one in the fully burnt products. In droplet combustion it is advantageous to employ an oxidiser-based reaction progress variable, which takes the following form [19, 25, 27, 29]:

$$c=\frac{\left(1-\xi\right)Y_{O\infty}-Y_O}{\left(1-\xi\right)Y_{O\infty}-\max?\left(0,\left[\xi_{st}-\xi\right]/\xi_{st}\right)Y_{O\infty}} \tag{17}$$

From Eq. 17 it is possible to derive a transport equation of c based on the transport equations for the oxidizer mass fraction Y_O and the mixture fraction ξ [9]:

$$\rho\frac{\partial c}{\partial t}+\rho u_j\frac{\partial c}{\partial x_j}=\nabla\cdot\left(\rho D\nabla c\right)+\dot{\omega}_c+\dot{S}_c+\dot{A}_c \tag{18}$$

where the first term on the right-hand-side arises due to molecular diffusion, the second represents reaction rate, the third is the source/sink term arising due to droplet evaporation, and the last is the cross-scalar dissipation term arising due to reactant inhomogeneity [19, 34, 35]. The cross-scalar dissipation term $\dot{A}_c$ in Eq. 18 arises due to mixture inhomogeneity [19, 34, 35], which, in this case, is induced by droplet evaporation. According to the definition of c (see Eq. 17), the definitions of $\dot{\omega}_c$, $\dot{S}_c$ and $\dot{A}_c$ depend on the local value of ξ. The reaction rate $\dot{\omega}_c$ of the reaction progress variable may be expressed as [19]:

$$\dot{\omega}_c = \begin{cases} -\frac{\xi_{st}\dot{\omega}_O}{[\xi(1-\xi_{st})Y_{O\infty}]} & , \xi \leq \xi_{st} \\ -\frac{\dot{\omega}_O}{[(1-\xi)Y_{O\infty}]} & , \xi > \xi_{st} \end{cases} \tag{19}$$

The expressions for $\dot{S}_c$ and $\dot{A}_c$ are given as [19]:

$$\dot{S}_c = \begin{cases} \frac{-\xi_{st}}{[(1-\xi_{st})\xi^2 Y_{O\infty}]}(\xi\dot{S}_O + (Y_{O\infty} - Y_O)\,\dot{S}_\xi) & , \xi \leq \xi_{st} \\ \frac{-1}{[(1-\xi)^2 Y_{O\infty}]}(\left(1-\xi\right)\dot{S}_O + Y_O\dot{S}_\xi) & , \xi > \xi_{st} \end{cases} \tag{20}$$

$$\dot{A}_c = \begin{cases} \frac{2\rho D}{\xi}\nabla c \cdot \nabla\xi & , \xi \leq \xi_{st} \\ \frac{-2\rho D}{(1-\xi)}\nabla c \cdot \nabla\xi & , \xi > \xi_{st} \end{cases} \tag{21}$$

where $\dot{S}_\xi = (\dot{S}_F - \dot{S}_O/s)/(Y_{F\infty} + Y_{O\infty}/s)$ is the droplet source/sink term in the mixture fraction transport equation and $\dot{S}_F = (1-Y_F)\,\Gamma_m$ and $\dot{S}_O = -Y_O\Gamma_m$ are the droplet source/sink terms in the fuel and oxidizer transport equations respectively and Γ_m is the source term in the mass conservation equation due to evaporation.

The molecular diffusion term in Eq. 18 can further be split into its normal and tangential components to yield [19]:

$$\nabla\cdot(\rho D\nabla c) = \vec{N}\cdot\nabla\left(\rho D\vec{N}\cdot\nabla c\right) - 2\rho D\kappa_m\,|\nabla c| \tag{22}$$

where D is the progress variable diffusivity $\vec{N} = -\nabla c/|\nabla c|$ is the flame normal vector, $\kappa_m = 0.5(\nabla\cdot\vec{N})$ is the arithmetic mean of the two principal curvatures of a given isosurface $c = c^*$. In Eq. 22 the first term on the right-hand-side gives the component of molecular diffusion normal to the flame front and the second term represents the tangential molecular diffusion component.

The transport equation of c can be recast in kinematic form in the following manner:

$$\frac{\partial c}{\partial t} + u_j\frac{\partial c}{\partial x_j} = S_d|\nabla c| \tag{23}$$

where S_d is the displacement speed which is the speed at which a given c isosurface moves normal to itself with respect to an initially coincident material surface. A comparison between Eqs. 18 and 23 yields:

$$S_d = \frac{\left[\nabla\cdot(\rho D\nabla c) + \dot{\omega}_c + \dot{S}_c + \dot{A}_c\right]}{\rho\,|\nabla c|} \tag{24}$$

Using Eq. 23 one obtains a transport equation for the Surface Density Function (SDF) (i.e. $|\nabla c|$) [36–38]:

$$\frac{\partial|\nabla c|}{\partial t} + V_j\frac{\partial|\nabla c|}{\partial x_j} = -\left(a_n + N_j\frac{\partial S_d}{\partial x_j}\right)|\nabla c| \tag{25}$$

where $V_j = u_j + S_d N_j$ is the j^{th} component of the propagation velocity of a given c isosurface, and $a_n = N_i N_j \partial u_i/\partial x_j$ is the flame normal strain rate. Furthermore, it can be shown that [38]:

$$\frac{1}{\Delta x_n}\frac{d\Delta x_n}{dt} = \left(a_n + N_j \frac{\partial S_d}{\partial x_j}\right) \tag{26}$$

where Δx_n is the distance between two neighbouring c isosurfaces. It is clear from Eqs. 25 and 26 that for $(a_n + N_j \partial S_d / \partial x_j) > 0$ the separation between c isosurfaces increases, whereas the magnitude of the SDF, $|\nabla c|$, decreases. Furthermore the evolution of an elemental flame surface area A may be given by [36]:

$$\frac{1}{A}\frac{dA}{dt} = a_T + 2S_d\kappa_m \tag{27}$$

where $a_T = \nabla.\vec{u} - a_n = (\delta_{ij} - N_i N_j)\partial u_i/\partial x_j$ is the tangential strain rate, $\nabla.\vec{u}$ is the dilatation rate and $K = a_T + 2S_d\kappa_m$ is the flame stretch rate. It is evident from Eqs. 25-27 that the statistical behaviours of dilatation rate $\nabla\vec{u}$; normal strain rate a_n ; tangential strain rate a_T ; normal strain rate induced by flame propagation $N_j\partial S_d/\partial x_j$ and curvature induced stretch $2S_d\kappa_m$ determine the scalar gradient and flame area generation in turbulent spray flames. The statistical behaviour of displacement speed S_d and its tangential strain rate a_T and curvature κ_m dependences for spray flames has been discussed elsewhere [19] and thus the current analysis will focus principally on the statistical behaviours of a_n , a_T, $N_j\partial S_d/\partial x_j$ and $2S_d\kappa_m$ in Section 4 of this paper.

3 Numerical Implementation

The present numerical investigation employs a widely-used three-dimensional compressible DNS code SENGA [19, 25, 27, 29, 39] which solves the standard transport equations of mass, momentum, energy and species in non-dimensional form. In SENGA the spatial discretisation for the internal grid points is carried out using a 10th order central difference scheme, but the order of differentiation drops gradually to a one-sided 2nd order scheme at the non-periodic boundaries [39]. The time advancement has been carried out using a low-storage third-order explicit Runge-Kutta scheme [40]. For the current investigation a rectangular computational domain of size $63.35D_0/S_{b(\phi_g=1)} \times 42.17D_0/S_{b(\phi_g=1)} \times 42.17D_0/S_{b(\phi_g=1)}$ has been considered where D_0 is the mass diffusivity in the unburned gas. For the present thermo-chemistry the Zel'dovich flame thickness $D_0/S_{b(\phi_g=1)}$ is equal to about $0.625\delta_{th}$ where $\delta_{th} = \left(T_{ad(\phi_g=1)} - T_0\right)/\max\left(\left|\nabla\hat{T}\right|\right)_L$ is the unstrained thermal laminar flame thickness of the stoichiometric laminar flame, and the subscript L refers to the values in an unstrained laminar premixed flame for the stoichiometric mixture. The simulation domain for the present analysis is discretised using a Cartesian grid of size $384 \times 256 \times 256$ which ensures a grid spacing which is fine enough to resolve both the flame thickness, δ_{th} and the Kolmogorov length-scale, η. The boundaries in the mean direction of flame propagation (i.e. x-direction) are considered to be partially non-reflecting, whereas the transverse (i.e. y- and z-) directions are taken to be periodic. The non-periodic boundary conditions are specified using the Navier-Stokes Characteristic Boundary Conditions (NSCBC) technique [41]. The droplets are distributed uniformly in space throughout the y- and z-directions and in the region $0.0 \leq xS_{b(\phi_g=1)}/D_0 \leq 16.53$ ahead of the flame. The reacting flow field is initialised based on the steady laminar solution obtained for the desired initial values

of droplet diameter, a_d and droplet equivalence ratio, ϕ_d. The steady laminar solution is generated using COSILAB [42], where the one-dimensional governing equations for the gas and liquid phases are solved in a coupled manner for spray flames where fuel is supplied in the form of mono-disperse droplets on the unburned gas side of the flame. Interested readers are referred to Ref. [14] for further information on the mathematical framework for generating steady state one-dimensional solutions of the laminar flame-droplet interaction for mono-disperse sprays. The initial turbulent velocity fluctuations have been generated using a standard pseudo-spectral method [43], and this field is superimposed on the steady laminar spray flame solution generated using COSILAB [42]. For the present analysis the unburned gas temperature is taken to be $T_0 = 300$K, which yields a heat release parameter $\tau = \left(T_{ad(\phi_g=1)} - T_0\right)/T_0 = 6.54$ under atmospheric pressure. For all simulations, the fuel is supplied purely in the form of mono-disperse droplets with non-dimensional diameters a_d/δ_{th}=0.06, 0.08, 0.10 for different values of droplet equivalence ratio: $\phi_d = 1.0, 1.25, 1.5, 1.7$ at a distance $10\delta_{th}$ from the point in the laminar flame at which $\hat{T} = 400$K, which corresponds to a non-dimensional temperature $T \approx 0.05$. The droplet number density ρ_N at $t = 0$ varies between $1.16 \leq (\rho_N)^{1/3}\ \delta_{th} \leq 2.27$, in the region $0.0 \leq xS_{b(\phi_g=1)}/D_0 \leq 16.53$. In all cases the liquid volume fraction remains much less than 0.01. In all cases droplets are supplied at the left-hand-side boundary to maintain a constant ϕ_d ahead of the flame. The droplets evaporate as they approach the flame front. Due to the relatively high volatility of n-heptane, evaporation commences immediately upon entry and the droplet diameter decreases by at least 50 %, 35 % and 25 % by the time it reaches the most reactive region of the flame for the initial a_d/δ_{th}=0.06, 0.08, 0.10 cases respectively, such that the volume of even the largest droplets is now less than half that of the cell volume, which validates the sub-grid point source treatment of droplets adopted for flame-droplet interactions analysed here since this study is concerned primarily with regions where reaction rate is non-negligible. The ratio of droplet diameter to grid spacing (i.e. $a_d/\Delta x$) remains smaller than unity and its value is comparable to several analyses [21, 22, 24, 25, 27, 30], which contributed significantly to the fundamental understanding of turbulent droplet-fuelled combustion. Using smaller droplets leads to complete evaporation of droplets ahead of the flame (as reported by Burgoyne and Cohen [5] and Neophytou and Mastorakos [14] by experimental and computational means, respectively), and thus gives rise to an analysis of turbulent flame propagation in stratified mixtures instead of flame-droplet interaction, which is the primary focus of this paper. This justifies the choice of the initial diameters of the cases considered here.

It is worth noting that the distance over which the reaction progress variable c changes from 0.01 to 0.99 is actually 2.5-3.0 times thicker than δ_{th} which provides the measure of highest temperature gradient within the flame. This means than more than 30 points span over the distance over which c changes from 0.01 to 0.99. In the present analysis, the droplet source terms $\dot{S}_\psi$ are tri-linearly interpolated from the droplet's sub-grid position, $\vec{x}_d$, to the eight surrounding nodes. This means that any possible numerical issues arising from relatively large droplets upstream of the flame are unlikely to affect the flame-droplet interaction and its statistics.

The simulations are carried out under both laminar flow conditions and for normalised root-mean-square (rms) turbulent velocities $u'/S_{b(\phi_g=1)} = 4.0$ and 7.5 with a non-dimensional longitudinal integral length-scale $L_{11}/\delta_{th} = 2.5$. This value of L_{11}/δ_{th} ensures that enough number of integral eddies are retained when the statistics are extracted. The ratio of droplet diameter to the Kolmogorov scale is $a_d/\eta \approx 0.3, 0.4, 0.5$ for $a_d/\delta_{th} \approx 0.06, 0.08, 0.1$ respectively for initial $u'/S_{b(\phi_g=1)} = 7.5$. The ratio of droplet

diameter to the Kolmogorov length scale a_d/η remains comparable to several previous analyses [21, 22, 24, 25, 27, 30]. The mean normalised inter-droplet distance s_d/η ranges between 0.0220 and 0.0432 (i.e. $0.0220 < s_d/\eta < 0.0432$) for the highest $u'/S_{b(\phi_g=1)}$ case. All simulations have been carried out until $t_{final} = \max(3t_{turb}, 4t_{chem})$, where $t_{turb} = L_{11}/u'$ is the initial turbulent eddy turnover time and $t_{chem} = D_0/S^2_{b(g=1)}$ the chemical timescale. This simulation time is either comparable to or greater than the simulation duration used in a number of recent DNS analyses [22, 24, 25, 27, 29–31, 44–47], which significantly contributed to the fundamental understanding of turbulent combustion. It was shown in Ref. [19] that the volume-integrated reaction rate, flame surface area and burning rate per unit area were not changing rapidly when the statistics have been extracted. This information is not repeated here for the sake of conciseness.

In order to obtain the Reynolds/Favre averaged value of a general quantity Q (i.e. $\bar{Q}$ and $\tilde{Q}$) the quantity Q is ensemble averaged over the y-z plane at a given x location. The statistical convergence of the Reynolds/Favre averaged values has been assessed by comparing the values obtained on full sample size with the corresponding values based on the half of the available sample size in the span-wise direction. In the next section the values based on full sample size will be reported for the sake of brevity.

4 Results & Discussion

The instanteneous distributions of non-dimensional temperature T, fuel mass fraction Y_F and reaction progress variable c at the central $x-z$ midplane at $t \approx 4t_{chem}$ are shown

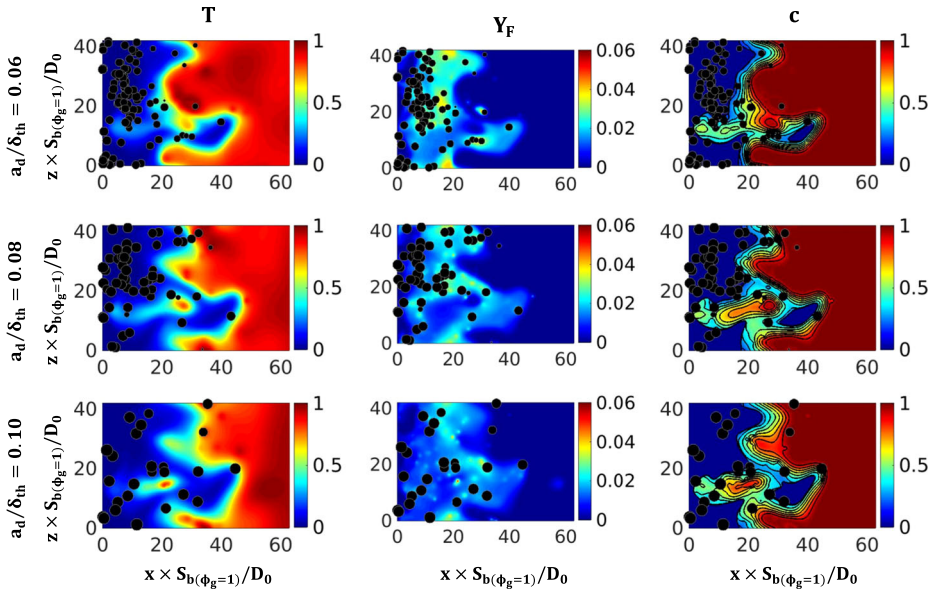

Fig. 1 (*Left to right*) Non-dimensional temperature, T, fuel mass fraction, Y_F, and reaction progress variable, c, (black contours show $c = 0.1, .., 0.9$ isosurfaces in steps of 0.1) fields at the central $x-z$ mid-plane in the case of $\phi_d = 1.0$ and $u'/S_{b(\phi_g=1)} = 7.5$ for (top to bottom) droplets with normalised initial diameter $a_d/\delta_{th} = 0.06, 0.08$ and 0.10 respectively. Droplet sizes are not shown to scale

in Fig. 1 for each droplet size with the droplet equivalence ratio $\phi_d = 1.0$ and initial $u'/S_{b(\phi_g=1)} = 7.5$. The droplets, which are depicted by black dots, are those residing in the cells immediately above or below the plane shown in the figure. It is evident from Fig. 1 that, the droplets reduce in size as they approach the flame due to evaporation. The degree of mixture inhomogoneity on the unburned gas side of the flame appears to increase with the droplet size. The gaseous fuel clouds surrounding individual droplets coalescing to form a single large cloud for small droplets, but this does not happen for larger droplets which are fewer in number and also evaporate more slowly. It is also noteworthy that several droplets of each size can be seen to have penetrated the flame front. The droplets continue to evaporate in the burnt gas region and some of the evaporated gaseous fuel eventually diffuses back towards the flame front. A comparison between the fuel mass fraction Y_F and reaction progress variable c fields indicate that, almost without exception, the inhomogeneous mixture arising from evaporation remains fuel-lean (i.e. $Y_F < Y_{Fst}$) on the unburned gas side. It can further be seen from Fig. 1 that the temperature of the burned gas in droplet cases is considerably smaller than the corresponding stoichiometric turbulent premixed flame and this reduction in burned gas temperature originates predominantly due to fuel-lean mode of combustion and also due to extraction of latent heat by the droplets. This is consistent with previous findings based on unsteady laminar and two-dimenional simulations [15–18].

The predominance of fuel-lean conditions observed in Fig. 1 can further be substantiated from Fig. 2a1-c1 which shows the probability density function (PDF) of ξ/ξ_{st} for the reaction progress variable range $0.10 \leq c \leq 0.99$. Figure 2a1 shows that, under laminar flow conditions, the chance of finding stoichiometric mixture (i.e. $\xi/\xi_{st} = 1.0$) is relatively high for all droplet sizes. However, the most likely outcome varies both with the droplet size and with droplet equivalence ratio. Small droplets with $\phi_d = 1.25$ are the combination most likely to produce a stoichiometric mixture. However, when ϕ_d is reduced (i.e. $\phi_d = 1.00$) the evaporated fuel is insufficient to produce a stoichiometric mixture and the mixture remains largely fuel-lean, whereas when ϕ_d is increased sufficiently (i.e. $\phi_d = 1.70$) the abundance of evaporated fuel in the absence of turbulent mixing leads to a high likelihood of finding fuel-rich mixture. In contrast, both medium and large droplets show extremely low likelihood of producing fuel-rich mixture, but considerable likelihood of fuel-lean mixture, such that the likelihood of finding stoichiometric mixture decreases with increasing droplet size. Furthermore, the effect of varying ϕ_d is much smaller for medium and large droplets. The reason for this is that the small droplets evaporate relatively quickly. Thus, on the one hand, under suitable conditions (e.g. $\phi_d = 1.25$) the system develops some of the physical characteristics of the equivalent gaseous homogeneous system, however, on the other hand, under unsuitable conditions (e.g. $\phi_d = 1.70$) regions of fuel-rich mixture are able to develop. Medium and large droplets are fewer in number (for constant ϕ_d) and evaporate more slowly such that they are likely to produce fuel-lean mixture (i.e. $\xi/\xi_{st} < 1.0$) for all ϕ_d investigated here. A further result of the low evaporation rate of the medium and large droplets is that increasing ϕ_d has less effect for these droplets than for the small droplets. The effects of chemical reaction and heat release are strong for $\xi/\xi_{st} \approx 1.0$ mixtures and thus the evaporation rate is expected to be high close to these regions. This eventually leads to the peak value of PDF of normalised mixture fraction at $\xi/\xi_{st} \approx 1.0$ in Fig. 2a1. Figures 2b1-c1 show the effect of turbulent mixing on the PDFs of normalised mixture fraction. It can be seen that, as the turbulent intensity increases, the likelihood of finding stoichiometric mixture decreases for all droplet cases. Similarly, the high likelihoods of finding fuel-lean mixture for small droplets with $\phi_d = 1.00$ and fuel-rich mixture for small droplets with $\phi_d = 1.70$ are both reduced due to more efficient mixing. The large variations arising due

to varying ϕ_d in the PDFs of small droplets seen under laminar flow conditions are much reduced under sufficiently turbulent flow conditions. Consequently, the PDFs for all droplet sizes are more similar under turbulent flow conditions than under laminar flow conditions. In Fig. 2a2-c2 the same PDFs are shown for a narrower range $0.10 \leq c \leq 0.90$. By comparing Fig. 2a2-c2 with Fig. 2a1-c1 it is apparent that the peak of PDF(ξ / ξ_{st}) at $\xi / \xi_{st} \approx 1.0$ arises principally from the region $c > 0.90$ due to high rate of droplet evaporation as a result of high temperature in the burnt gas region. Figures 2a2-c2 show that most parts of

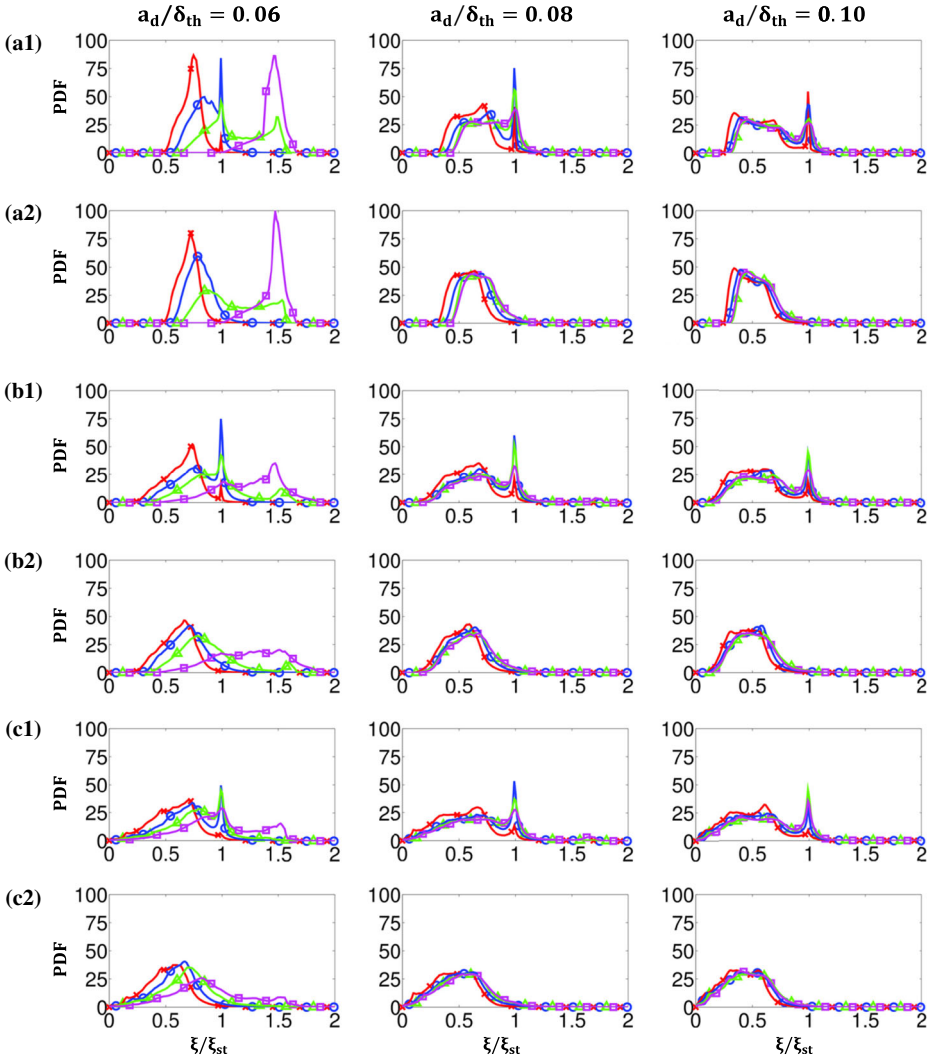

Fig. 2 PDFs of ξ/ξ_{st} in the regions corresponding to (rows a1,b1,c1) $0.10 \leq c \leq 0.99$ and (rows a2,b2,c2) $0.10 \leq c \leq 0.90$ under (rows a1,a2) laminar flow conditions and turbulent flow conditions with initial (rows b1,b2) $u' / S_{b(\phi_g=1)} = 4.0$ and (rows c1,c2) $u' / S_{b(\phi_g=1)} = 7.5$ for initial droplet diameters (*columns left to right*) $a_d / \delta_{th} = 0.06, 0.08, 0.10$ and for droplet equivalence ratios: $\phi_d = 1.00$ (*red cross*), 1.25 (*blue circle*), 1.50 (*green triangle*) and 1.70 (*magenta square*)

the flame become increasingly fuel-lean with increasing droplet diameter. Furthermore, the PDFs of the broader range ($0.10 \leq c \leq 0.99$) at time $t = 0$ (not shown) indicate an even greater probability (up to an order of magnitude larger) for $\xi / \xi_{st} < 1.0$. It can be seen from the PDFs of ξ/ξ_{st} in Fig. 2 that a large range of mixture fraction values are obtained in gaseous phase. Thus, it is not possible to identify a single representative mixture fraction ξ for the gaseous phase combustion. As PDF(ξ / ξ_{st}) exhibits peak values at $\xi/\xi_{st} \approx 1.0$ for most of the droplet cases considered here, several quantities in droplet cases are compared to the corresponding stoichiometric premixed flame quantities later in this paper.

The reaction progress variable c fields in Fig. 1 show important differences with the change of initial droplet diameter a_d. It can be seen from Fig. 1 that c isosurfaces representing the preheat zone (e.g. $c < 0.5$) are more wrinkled than the isosurfaces in the reaction zone (e.g. $0.7 < c < 0.9$) for all cases considered here. This behaviour is typical of thickened flame regime of combustion (e.g. thin reaction zones regime) where turbulent eddies can penetrate into the flame, but decay before entering into the reaction zone, which allows for sustained combustion without extinction. The regime of combustion can be characterised with the help of Karlovitz number $Ka = (u'/S_{b(_g)})^{3/2} (L_{11} S_{b(_g)}/D_0)^{-1/2}$, which provides a measure of the ratio of flame thickness to the Kolmogorov length scale [48]. One obtains a Karlovitz number of 9.0 (3.5) for the values of $u'/S_{b(\phi_g=1)} = 7.5$ (4.0) and $L_{11} / \delta_{th} = 2.5$. The value of Karlovitz number is likely to be greater than 9.0 under fuel-lean conditions, which suggests that combustion in all cases takes place nominally within the distributed reaction zone regime. In this regime of combustion the energetic turbulent eddies penetrate into the flame and disturb the preheat zone significantly, but flame extinction is spared if the Kolmogorov length scale is greater than the reaction zone thickness.

It can further be seen from Fig. 1 that for the smallest droplets most c isosurfaces lie very close together, whereas, the isosurfaces are increasingly separated from each other for the medium and large droplets, indicating a broadening of the flame in these cases. The thickening of the reaction zone can be confirmed from Fig. 3, which shows the variation of a quantity Δ which is the ratio of the mean value of the surface density function (SDF) (i.e. $|\nabla c|$) conditional on c for the droplet cases to the corresponding quantity obtained for stoichiometric turbulent premixed flame under similar unburned gas turbulence (i.e. $\Delta = \langle |\nabla c| \rangle_c / \langle |\nabla c|_{premix} \rangle_c$, where $\langle ... \rangle_c$ indicates ensemble-averaged values conditional on c and the subscript 'premix' is used for referring to the values in the corresponding stoichiometric premixed flame). Dimensionally the inverse of the normalised SDF, $|\nabla c|$ can be understood as a measure of the turbulent flame thickness (i.e. $|\nabla c| \sim 1/\delta$, where δ is the local flame thickness). It can be seen from Fig. 3 that Δ predominantly assumes a value smaller than unity throughout the flame front (values of Δ greater than unity for $c \approx 0$ and $c \approx 1$ arise since $\langle |\nabla c|_{premix} \rangle_c \approx 0$ at these locations), which indicates a thicker flame in comparison to a stoichiometric premixed laminar flame in spite of a peak value of PDF of normalised mixture fraction at $\xi/\xi_{st} \approx 1.0$. It has already been shown elsewhere [19] that the peak value of $\langle |\nabla c| \rangle_c$ for turbulent stoichiometric premixed flames remains comparable to that of the planar laminar stoichiometric premixed flame. This indicates that the flame thickness in droplet cases is greater than the stoichiometric premixed flame thickness (i.e. $\delta > \delta_{th}$). As combustion takes place predominantly under fuel-lean mode (see Fig. 2), the flame thickness $\varphi\delta \sim D/S_{b(g)}$ is expected to be greater than that in the stoichiometric premixed flame. As a result, Δ remains smaller than unity for all droplet cases considered here.

Almost without exception, Δ increases with increasing ϕ_d for all droplet cases, indicating that an increase in ϕ_d leads to a corresponding decrease in flame thickness. The greatest

effect (i.e. the greatest decrease in flame thickness due to an increase in ϕ_d) can be seen in the case of small droplets, whereas for medium and large droplets the effect is smaller. The exception being small droplets under laminar flow conditions and $\phi_d = 1.70$, which, due to the fuel-rich nature of the mixture, has the thickest flame of all. Finally, for constant turbulent intensity and constant ϕ_d, the flame thickness increases with increasing droplet size. This can also be seen in Fig 1.

It has already been shown in Fig. 2 that stoichiometric or fuel-rich mixture is most likely to be found in the region corresponding to $c > 0.90$, whereas most of the unburnt gas region remains fuel-lean. Figure 4 shows the distribution and variation of non-dimensional temperature, T, reaction progress variable,c, fuel mass fraction, Y_F, normalised fuel reaction rate magnitude, $|\dot{\omega}_F|^* = |\dot{\omega}_F| \times \delta_{th}/\rho_0 S_{b(\phi_g=1)}$, and normalised surface density function, $|\nabla c| \times \delta_{th}$, with mixture fraction, ξ. Figure 4 reveals the difference in behaviour of these quantities between regions corresponding to $\xi < \xi_{st}$ and those corresponding to $\xi \approx \xi_{st}$. The left hand pane of Fig. 4 shows the scatter of non-dimensional temperature, T, reaction progress variable, c, fuel mass fraction, Y_F, normalised fuel reaction rate magnitude,

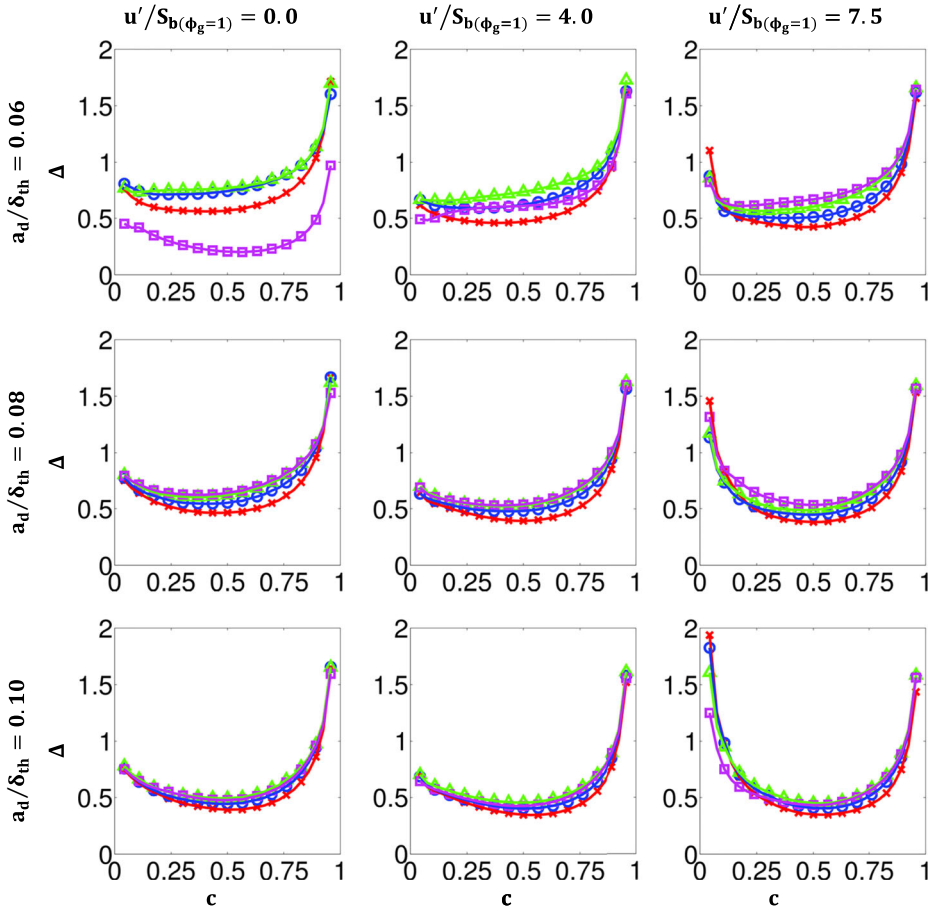

Fig. 3 Variation of normalised surface density function, $\Delta = \langle|\nabla c|\rangle_c / \langle|\nabla c|_{premix}\rangle_c$, with c for all droplet cases with ϕ_d= 1.00 (*red cross*), 1.25 (*blue circle*), 1.50 (*green triangle*) and 1.70 (*magenta square*)

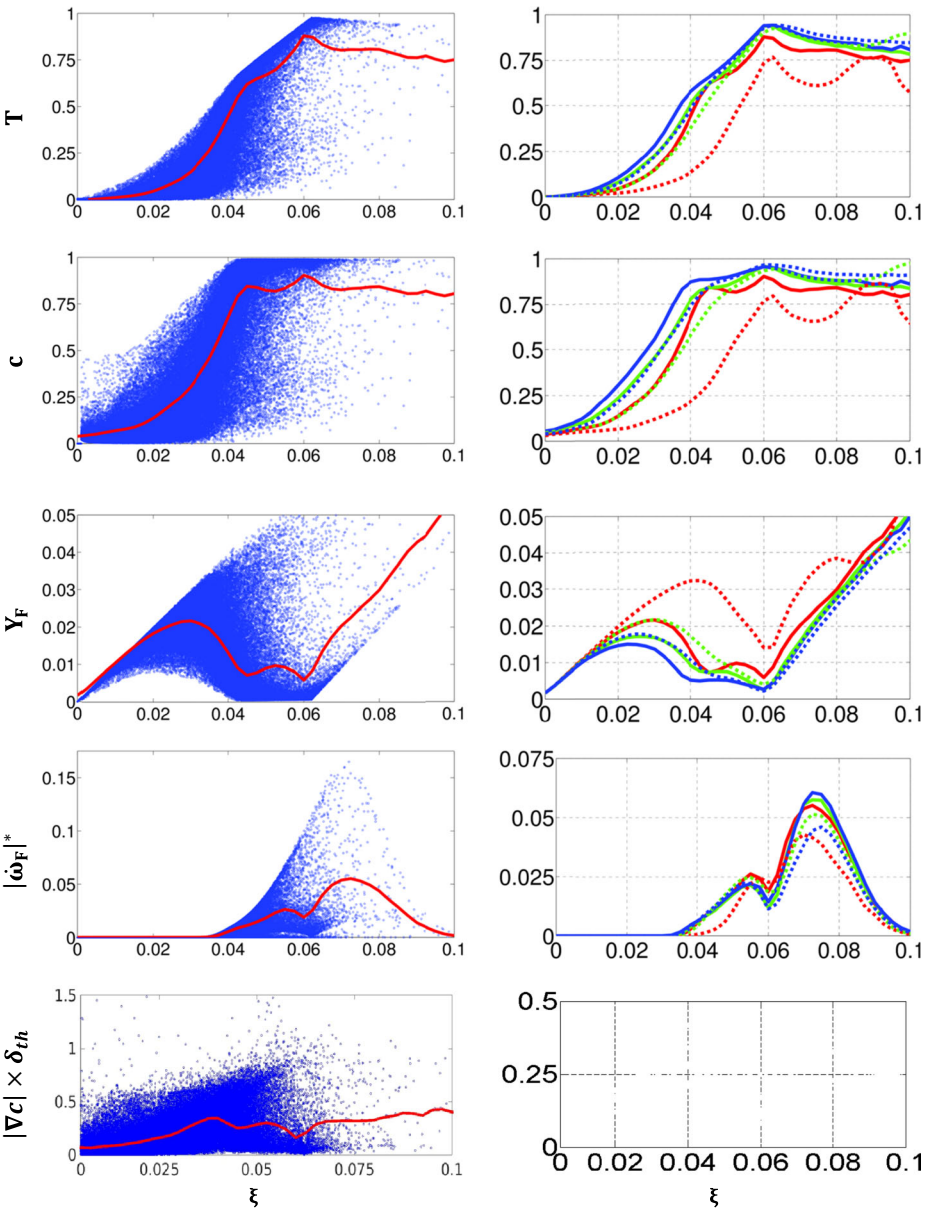

Fig. 4 (*Left column*) Scatter plots of variation with ξ of non-dimensional temperature, T, reaction progress variable,c, fuel mass fraction, Y_F, normalised fuel reaction rate,$|\dot{\omega}_F|^* = |\dot{\omega}_F| \times \delta_{th}/\rho_0 S_{b(\phi_g=1)}$, and normalised surface density function, $|\nabla c| \times \delta_{th}$, for droplet case with $a_d/\delta_{th} = 0.06$ and $\phi_d = 1.00$ under turbulent flow conditions $u'/S_{b(\phi_g=1)} = 7.5$, overlaid with variation of averaged values conditional on ξ (*red line*). (*Right column*) Variation of averaged values of variables conditional on ξ for droplet cases $a_d/\delta_{th} = 0.06$(*red*), 0.08(*green*)and0.10(*blue*) with $\phi_d = 1.00$ (*solid line*) and 1.70 (*dashed line*) under $u'/S_{b(\phi_g=1)} = 7.5$. For the plots involving the normalised surface density function, $|\nabla c| \times \delta_{th}$, only the samples corresponding to $0.01 \leq c \leq 0.99$ have been considered

$|\dot{\omega}_F| \times \delta_{th}/\rho_0 S_{b(\phi_g=1)}$, and normalised surface density function, $|\nabla c| \times \delta_{th}$, with ξ for one droplet case ($a_d / \delta_{th} = 0.06$, $\phi_d = 1.00$ and $u' / S_{b(\phi_g=1)} = 7.5$). The scatter of each quantity is overlaid with the ensemble-averaged value of the quantity conditional on ξ (henceforth referred to as $\langle Q \rangle_\xi$, which indicates the ensemble-averaged value of a general quantity Q conditional on ξ)[1] It is worth noting that these conditional averages are evaluated using the data from the whole domain and thus these values are affected by the relative length of the domain upstream and downstream of the flame, compared to the flame thickness. Thus, these conditional average values should only be considered for the purpose of qualitative comparison between different cases in the same configuration. It can be seen that both the non-dimensional temperature and the reaction progress variable rise monotonically with ξ until they peak around $\xi \approx \xi_{st} = 0.0621$. It is furthermore clear that the vast majority of samples are fuel-lean, as anticipated from Figs. 1-2. A closer examination shows that the gradient of the slope of temperature conditionally averaged on mixture fraction $\langle T \rangle_\xi$ is higher for $\xi < 0.04$ than for $0.04 < \xi < 0.06$. This arises due to the fact that the mixtures with $\xi < 0.03$ are non-flammable. The increase of evaporation as the flame is approached is accompanied by the absorption of latent heat, which also acts to mitigate the increase in the gas temperature. Reaction progress variable increases rapidly with ξ at first. The increase slows down greatly at $\xi \approx 0.04$ and eventually peaks at a maximum value near $\xi = \xi_{st}$. The change in gradient of the reaction progress variable arises from its dependence on the oxidiser mass fraction (see Eq. 17), which in turn is dependent on the fuel mass fraction, such that an increase in Y_F leads to a decrease in Y_O but also increases the value of mixture fraction ξ. Therefore the combined effects of the decrease in Y_O and increase in ξ (as a result of the increase in fuel mass fraction Y_F) govern the reaction progress variable c in the preheat zone. It can be seen from Fig. 4 that Y_F increases initially with ξ due to droplet evaporation. This continues until the fuel reaction rate becomes non-negligible ($\xi \approx 0.04$) and fuel begins to be consumed, thereby leading indirectly to a change in the slope of c variation with ξ. Between $0.04 < \xi < 0.06$ the conditional average of Y_F is consistently low. This is due to the high rate of fuel consumption which occurs in this region, as can be seen from the variation of $\langle |\dot{\omega}_F| \rangle_\xi \times \delta_{th}/\rho_0 S_{b(\phi_g=1)}$. Finally, the scatter of $|\nabla c| \times \delta_{th}$ and the conditionally-averaged value $\langle \nabla c \rangle_\xi \times \delta_{th}$ are shown in Fig. 4. They remain consistently below unity, indicating a thicker flame than is found in stoichiometric premixed flames, as has been shown in Fig. 3.

The right hand pane of Fig. 4 shows the variation of the values of the aforementioned quantities conditionally averaged on ξ for a number of droplet cases: $a_d / \delta_{th} = 0.06$, 0.08 and 0.10 with $\phi_d = 1.00$ and 1.70 under turbulent flow conditions $u' / S_{b(\phi_g=1)} = 7.5$. In all cases shown here and for all quantities considered here the same qualitative trend is observed for the conditional averages as was seen in the case shown in the left hand pane. The non-dimensional temperature and reaction progress variable both exhibit higher values for larger droplet size and smaller droplet equivalence ratio. Conversely, $\langle Y_F \rangle_\xi$ increases both with smaller droplet size and with increasing ϕ_d. Both of these trends are once again due to the evaporation rate which is higher for small droplets and for larger numbers of the same size droplets (i.e. higher ϕ_d). In all cases considered here the fuel

[1] The variations of these quantities as a function of c have been presented elsewhere [19] and thus are not repeated here.

reaction rate magnitude exhibits a minimum near $\xi \approx 0.06$ and a maximum near $\xi \approx 0.07$. However, at $\xi \approx 0.06$ it is the largest droplets that exhibit the lowest minimum, whereas at $\xi \approx 0.07$ they exhibit the highest maximum. Finally, the variations of $\langle|\nabla c|\rangle_\xi \times \delta_{th}$ evaluated using the samples corresponding to $0.01 \leq c \leq 0.99$ show that, for $\xi < 0.03$ lower values are obtained for smaller droplets and for higher ϕ_d, whereas for $\xi > 0.04$ higher values are obtained for those cases. This shows that small droplets with high ϕ_d possess thicker flames for low ξ and thinner flames for high ξ than large droplets with low ϕ_d

The mode of combustion in gaseous phase can be characterised by means of a flame index: $FI = \nabla Y_F \cdot \nabla Y_O / |\nabla Y_F||\nabla Y_O|$ [49], where a positive flame index (i.e. $FI > 0$) indicates a premixed mode of combustion and a negative value (i.e. $FI < 0$) a non-premixed mode. It is expected that the inhomogeneities arising due to droplet evaporation will induce a non-premixed mode of combustion. It has already been shown in Ref. [19] that the relative contributions of premixed and non-premixed modes of combustion in terms of percentages of total heat release vary with u', a_d and ϕ_d, where the heat release due to combustion may be expressed as $H_\varphi|\dot{\omega}_F|$ (i.e. the heat release term in the energy conservation equation). Figures 5-6 show the scatter of $H_\varphi|\dot{\omega}_F|$ and conditional ensemble averaged values (i.e. $\langle H_\phi\,|\dot{\omega}_F|\rangle_c$ and $\langle H_\phi \dot{\omega}_F\rangle_\xi$) due to $FI > 0$ and $FI < 0$ as functions of c and ξ respectively for a number different droplet: $a_d \,/\delta_{th} = 0.06, 0.08$ and 0.1 with $\phi_d = 1.00$ and 1.70 under turbulent flow conditions $u' \,/S_{b(\phi_g=1)} = 7.5$. This heat release due to combustion arises only from the reaction zone so the non-zero contributions of $H_\varphi|\dot{\omega}_F|$ arise only from the reaction zone. Thus, the non-zero contributions of $H_\varphi|\dot{\omega}_F|$ arising from $FI > 0$ and $FI < 0$ are physical, and not artefacts of droplet evaporation. The scatter plots in all cases in Fig. 5 show that premixed mode combustion is predominant at lower values of c, whereas non-premixed mode combustion dominates at $c \approx 1.0$. This is consistent with Fig. 2 in which it was shown that the high probability of finding $\xi \approx \xi_{st}$ originates from the region corresponding to $c > 0.9$. The high values of c at $\xi \approx \xi_{st}$ arises due to the diffusion-type flame which develops as a result of droplet evaporation in the burnt gas region and the subsequent back-diffusion of the evaporated fuel (see also Ref [19]). The variations of the heat release in the premixed stoichiometric flame are shown together with the $\phi_d = 1.00$ droplet cases and the curve described by these values clearly divides the droplet scatter into premixed and non-premixed modes. The premixed mode combustion in the droplet cases is predominantly fuel-lean and, consequently, releases less heat compared to the premixed stoichiometric flame, whereas the non-premixed mode combustion takes place in regions where the mixture is close to $\xi \approx \xi_{st}$ or even slightly fuel-rich giving rise to greater heat release than the premixed stoichiometric flame. Furthermore, comparing $\langle H_\phi\,|\dot{\omega}_F|\rangle_c$ from the premixed stoichiometric flame with that of both modes of combustion in the droplet cases shows that the heat release in the premixed stoichiometric flame is far greater than in any of the droplet cases. This is due once again to the predominantly fuel-lean nature of the droplet cases. Finally, the scatter plots in Figs. 5 and 6 show that the number of samples arising due to premixed mode combustion appears to decrease with increasing droplet size, in contrast to the number arising due to non-premixed mode combustion which appears to increase with increasing droplet size. Similarly, the conditional average of heat release $\langle H_\phi\,|\dot{\omega}_F|\rangle_c$ and $\langle H_\phi\,|\dot{\omega}_F|\rangle_\xi$ due to non-premixed mode combustion can be seen to increase with increasing droplet size and increasing droplet equivalence ratio. Figure 6 shows that, for all cases considered here, the majority of non-premixed mode combustion takes place close to $\xi \approx \xi_{st}$ or under fuel-rich conditions, whereas the majority of premixed mode combustion takes place where $\xi < \xi_{st}$. This is made even clearer by the conditional averages of heat release rate which indicate that, in most cases, the heat release rate due to premixed mode combustion dominates where $\xi < 0.05$, but that due to non-premixed mode combustion

dominates where $\xi > 0.06$. Finally, the droplet case $a_d/\delta_{th} = 0.06$ and $\phi_d = 1.70$ is an exception to this trend. It arises due to the quicker evaporation of the small droplets and their abundance at this high value of ϕ_d. This leads to conditions approaching $\xi \approx \xi_{st}$ even in the premixed mode combustion.

The physical reasons behind the thickening of spray flames in comparison to a stoichiometric premixed flame can be understood in detail from the statistical behaviours of dilatation rate $\nabla\vec{u}$; normal strain rate a_N ; tangential strain rate a_T ; normal strain rate induced by flame propagation $N_j\partial S_d/\partial x_j$ and curvature induced stretch $2S_d\kappa_m$ (see Eqs. 25-27). The statistical behaviour of displacement speed S_d and its tangential strain rate a_T and curvature κ_m dependence was discussed in detail in [19] and thus the current analysis will focus next on the statistical behaviours of $\nabla\vec{u}$, a_N, a_T, $N_j\partial S_d/\partial x_j$ and $2S_d\kappa_m$.

The variations of the conditional averaged values of $\nabla\vec{u}$, a_N and a_T conditional on c (i.e. $\langle\nabla\cdot\vec{u}\rangle_c$, $\langle a_n\rangle_c$ and $\langle a_T\rangle_c$) are shown for droplet cases with $a_d/\delta_{th} = 0.06, 0.08, 0.10$ and $\phi_d = 1.00$ and 1.70 under laminar and turbulent flow conditions with initial $u'/S_{b(\phi_g=1)} =$ 4.0 and 7.5. For all cases $\langle\nabla\cdot\vec{u}\rangle_c$ shows predominantly positive values due to chemical heat

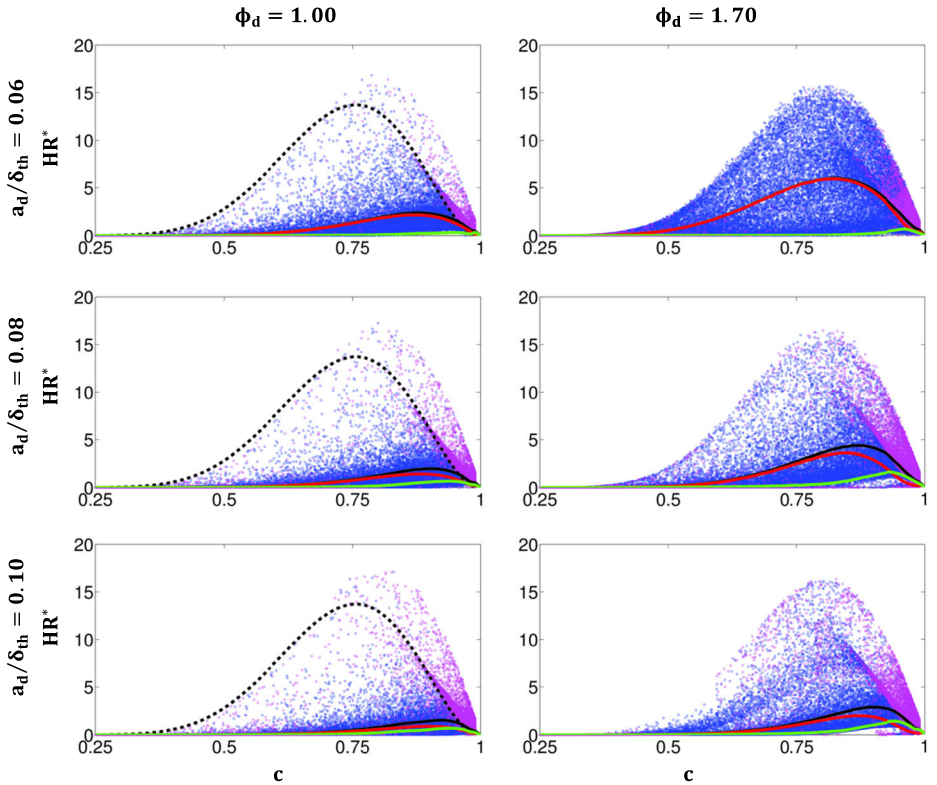

Fig. 5 Scatter plots of variation of normalised heat release, $HR^* = H_\varphi|\dot{\omega}_F| \times \delta_{th}/C_p(T_0)\rho_0 S_{b(\phi_g=1)}$, with c for droplet cases with (*top to bottom rows*) $a_d/\delta_{th} = 0.06, 0.08, 0.10$ and (*left to right columns*) $\phi_d = 1.00, 1.70$. Scatter arising due to FI > 0 and FI < 0 modes of combustion are shown in blue and magenta respectively. The variation of $\langle HR^*\rangle_c$ with c arising due FI > 0, FI < 0 and both modes of combustion are shown: FI > 0 (*red line*), FI < 0 (*green line*) and both (*solid black line*). The variation of $\langle HR^*\rangle_c$ with c for the corresponding stoichiometric premixed case is shown (*dashed black line*)

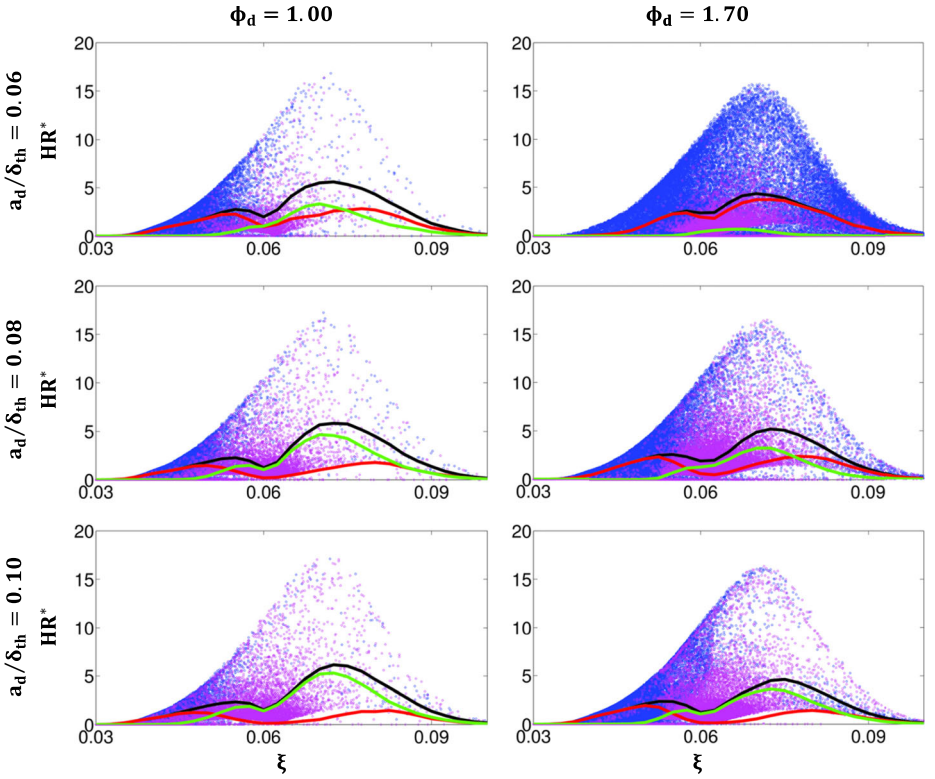

Fig. 6 Scatter plots of variation of normalised heat release, $HR^* = H_\varphi|\dot{\omega}_F| \times \delta_{th}/C_p(T_0)\rho_0 S_{b(\phi_g=1)}$ with ξ for droplet cases with (*top to bottom rows*) $a_d/\delta_{th} = 0.06, 0.08, 0.10$ and (*left to right columns*) $\phi_d = 1.00, 1.70$. Scatter arising due to FI > 0 and FI < 0 are shown in blue and magenta respectively. The variation of $\langle HR^* \rangle_\xi$ with ξ arising due to FI > 0, FI < 0 and both modes of combustion are shown: FI > 0 (*red line*), FI < 0 (*green line*) and both (*black line*)

release and the peak value is obtained at a location which is slightly skewed towards the burned gas side (i.e. $c \approx 0.75$). The peak value of $\langle \nabla \cdot \vec{u} \rangle_c$ decreases with increasing droplet size for all droplet cases and it increases with increasing ϕ_d for $a_d/\delta_{th} = 0.08$ and 0.1. However, for small droplets (i.e. $a_d/\delta_{th} = 0.06$ case) the maximum value of $\langle \nabla \cdot \vec{u} \rangle_c$ also depends strongly on the turbulence intensity $u'/S_{b(\phi_g=1)}$. Under laminar flow, $\phi_d = 1.70$ exhibits the lowest peak value of $\langle \nabla \cdot \vec{u} \rangle_c$ for $a_d/\delta_{th} = 0.06$, but, for sufficiently high turbulence intensity, it exhibits the highest peak value of $\langle \nabla \cdot \vec{u} \rangle_c$. This is due to the relative ease of evaporation of small droplets, which leads to regions of non-combustible fuel-rich mixture in the absence of sufficiently strong turbulent mixing and thus the effects of thermal expansion due to chemical heat release remain weak. However, for $a_d/\delta_{th} = 0.08$ cases $\langle \nabla \cdot \vec{u} \rangle_c$ in turbulent cases remains comparable to that in the laminar flow conditions for $\phi_d = 1.0$ cases but the peak value of $\langle \nabla \cdot \vec{u} \rangle_c$ in turbulent cases remains smaller than the corresponding laminar case for $\phi_d = 1.70$. This behaviour is also present in the $a_d/\delta_{th} = 0.10$ cases but to a much smaller extent than in the $a_d/\delta_{th} = 0.08$ cases. Turbulent mixing and heat transfer create relatively favourable conditions for evaporation, which extracts latent heat from the

gaseous phase and thus acts to reduce the peak value of $\langle \nabla \cdot \vec{u} \rangle_c$ in turbulent cases in comparison to that in the laminar case. The favourable condition for evaporation for high values of turbulence intensity $u' / S_{b(\phi_g=1)}$ leads to significant extraction of latent heat from the gaseous phase, which gives rise to the negative values of $\langle \nabla \cdot \vec{u} \rangle_c$ at the leading edge of the flame front for the cases with $u' / S_{b(\phi_g=1)} = 7.5$.[2] For unstrained freely propagating laminar flames the normal strain rate a_n assumes an almost identical value to that of the dilatation rate $\nabla \vec{u}$, and thus the tangential strain rate $a_T = \nabla \vec{u} - a_N$ remains negligible. Figure 7 suggests that the behaviour of $\langle a_n \rangle_c$ is strongly dependent on turbulence intensity $u' / S_{b(\phi_g=1)}$ and ϕ_d. For initial $u' / S_{b(\phi_g=1)} = 4.0$ cases $\langle a_n \rangle_c$ remains negative on both unburned and burned gas sides of the flame front for all droplet cases and it becomes positive only in the regions where $\nabla \vec{u}$ assumes high positive values. The extent of positive contribution of a_N for $\phi_d = 1.70$ is greater than in $\phi_d = 1.0$ for all droplet sizes and $u' / S_{b(\phi_g=1)}$. By contrast, an increase in turbulence intensity $u' / S_{b(\phi_g=1)}$ leads to an increase in the magnitude of negative contribution of a_N. The normal strain rate can be expressed as:

$$a_N = e_\alpha \cos^2\theta_\alpha + e_\beta \cos^2\theta_\beta + e_\gamma \cos^2\theta_\gamma \tag{28}$$

where e_α, e_β and e_γ are the most extensive (i.e. positive), intermediate and most compressive (i.e. negative) principal strain rate respectively and θ_α , θ_β and θ_γ are angles between ∇c and the eigenvectors associated with e_α, e_β and e_γ respectively. It was demonstrated earlier [50–52] that ∇c aligns collinearly with the eigenvector direction corresponding to e_γ in the region with weak heat release, but this alignment changes to the direction corresponding to e_α in the region with strong heat release, in which case the strain rate induced by flame normal acceleration overcomes background turbulent straining [50, 51]. According to Eq. 28 one obtains a positive value of a_N because of predominant collinear alignment between ∇c and e_α. By contrast, one obtains predominantly negative values of a_N when ∇c predominantly aligns with e_γ under the action of strong turbulent straining in which case it dominates over the strain rate induced by flame normal acceleration [50, 52]. Turbulent straining strengthens with increasing $u' / S_{b(\phi_g=1)}$ for a given value of integral length scale and thus the probabilities of finding collinear alignment between ∇c and e_γ and thus negative values of a_N are greater in the initial $u' / S_{b(\phi_g=1)} = 7.5$ cases than in $u' / S_{b(\phi_g=1)} = 4.0$ cases. The increase in droplet equivalence ratios ϕ_d increases the probability of obtaining flammable fuel-air mixture (especially stoichiometric mixture) in turbulent droplet cases (see Fig. 2). Thus the influences of strain rate induced by flame normal acceleration strengthen with increasing ϕ_d and as a result the probabilities of finding collinear alignment between ∇c and e_α and thus positive values of a_N are greater in the $\phi_d = 1.70$ cases than in $\phi_d = 1.0$ cases.

The relative magnitudes of $\nabla \vec{u}$ and a_N determine the magnitude of tangential strain rate $a_T = \nabla \vec{u} - a_N$. The value of $\langle a_T \rangle_c = \langle \nabla \cdot \vec{u} \rangle_c - \langle a_N \rangle_c$ increases with $u' / S_{b(\phi_g=1)}$ and $\phi_d = 1.0$. The high positive values of $\nabla \vec{u}$ is principally responsible for high values of tangential strain rate $a_T = \nabla \vec{u} - a_N$ for high ϕ_d turbulent cases. The high magnitude of negative value of a_N is principally responsible for high values of tangential strain rate $a_T = \nabla \vec{u} - a_N$ for high values of $u' / S_{b(\phi_g=1)}$. It has been found that the ensemble averaged values of $\nabla \cdot \vec{u}$, a_T and

[2] The flow under consideration takes place under low Mach number and, thus, the non-zero values of dilatation rate $\nabla \vec{u}$ arise only because of density change due to temperature change. In the current problem the density change can take place only due to chemical reaction or extraction of latent heat. In the leading edge of flame only the latent heat effect is present in the absence of chemical reaction.

a_N conditional on ξ (i.e. $\langle \nabla \cdot \vec{u} \rangle_\xi$, $\langle a_n \rangle_\xi$ and $\langle a_T \rangle_\xi$) assume high values close to $\xi \approx \xi_{st}$ for small droplets with $\phi_d = 1.00$ and 1.70 (not shown here for conciseness). This behaviour becomes less prominent with increasing droplet diameter.

The variation of $\langle a_N \rangle_c$ and $\langle N_j \partial S_d / \partial x_j \rangle_c$ and its components arising from different components of the displacement speed (i.e. $\langle N_j \partial S_i / \partial x_j \rangle_c$ where i = r, t, n, z) conditional on c for the stoichiometric premixed cases and for droplet cases with $a_d / \delta_{th} = 0.06, 0.08, 0.10$ are shown in Fig. 8 for $\phi_d = 1.00$ and 1.70 in the case of turbulent flow conditions with initial $u' / S_{b(\phi_g=1)} = 4.0$ and 7.5. The quantity $\langle N_j \partial S_r / \partial x_j \rangle_c$ remains active only in the region given by $0.5 < c < 1.0$ and it assumes negative values. Thus the normal strain rate induced by reaction component of displacement speed acts to reduce the normal strain rate and thus it tries to reduce the distance between two c isosurfaces (see Eqs. 25 and 26). This

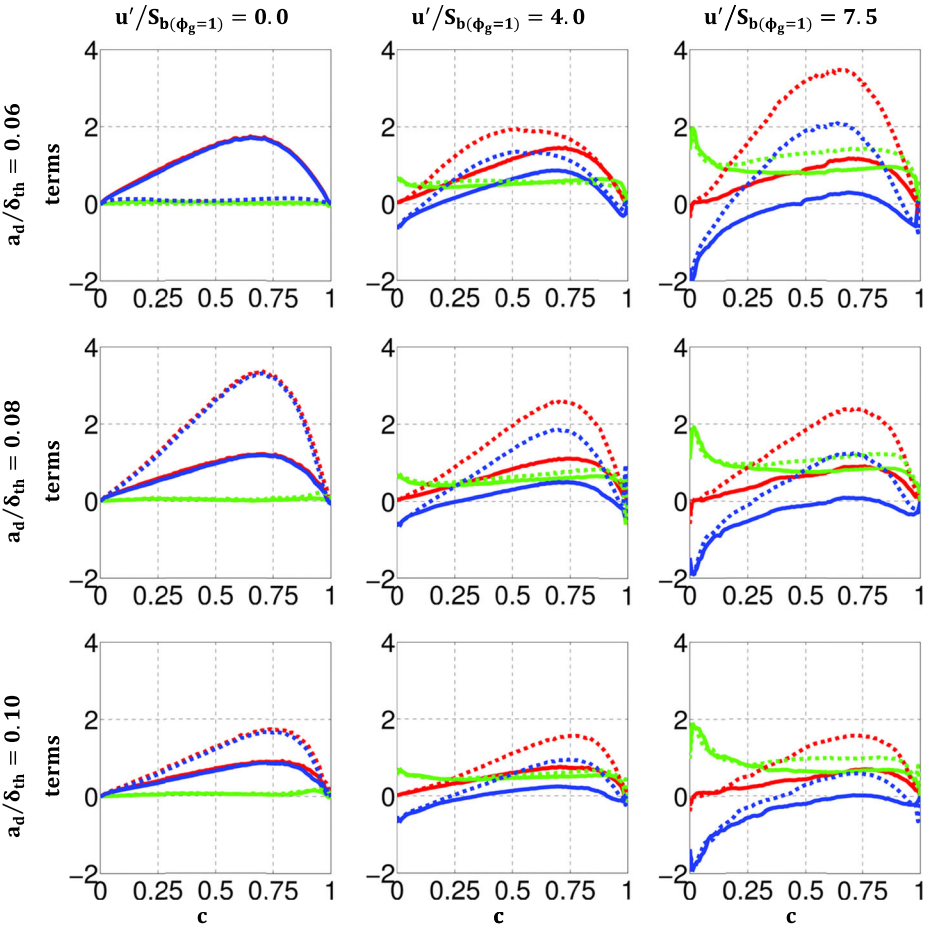

Fig. 7 Variation of conditional averages of dilatation rate $\langle \nabla \cdot \vec{u} \rangle_c$ (*red*), tangential strain rate $\langle a_T \rangle_c$ (*green*), and normal strain rate $\langle a_N \rangle_c$ (*blue*), with c for droplet cases (*top to bottom rows*) with $a_d / \delta_{th} = 0.06, 0.08, 0.10$ and $\phi_d = 1.00$ (*solid lines*) and 1.70 (*dashed lines*) under (column 1) laminar flow conditions and (columns 2-3) turbulent flow conditions $u' / S_{b(\phi_g=1)} = 4.0, 7.5$. Terms have been normalised by $\delta_{th} / S_{b(\phi_g=1)}$

component is more strongly negative in the stoichiometric premixed cases than in the droplet cases, due to higher chemical reaction rate gradient in the stoichiometric premixed cases. For all droplet cases considered here this component becomes more strongly negative for higher values of ϕ_d due to strengthening the effects of chemical reaction (and thus higher magnitude of S_r) as a result of higher availability of gaseous fuel. This component (i.e. $\langle N_j \partial S_r / \partial x_j \rangle_c$) is balanced in the stoichiometric premixed cases by the component arising from the normal diffusion component of displacement speed (i.e. $\langle N_j \partial S_n / \partial x_j \rangle_c$),

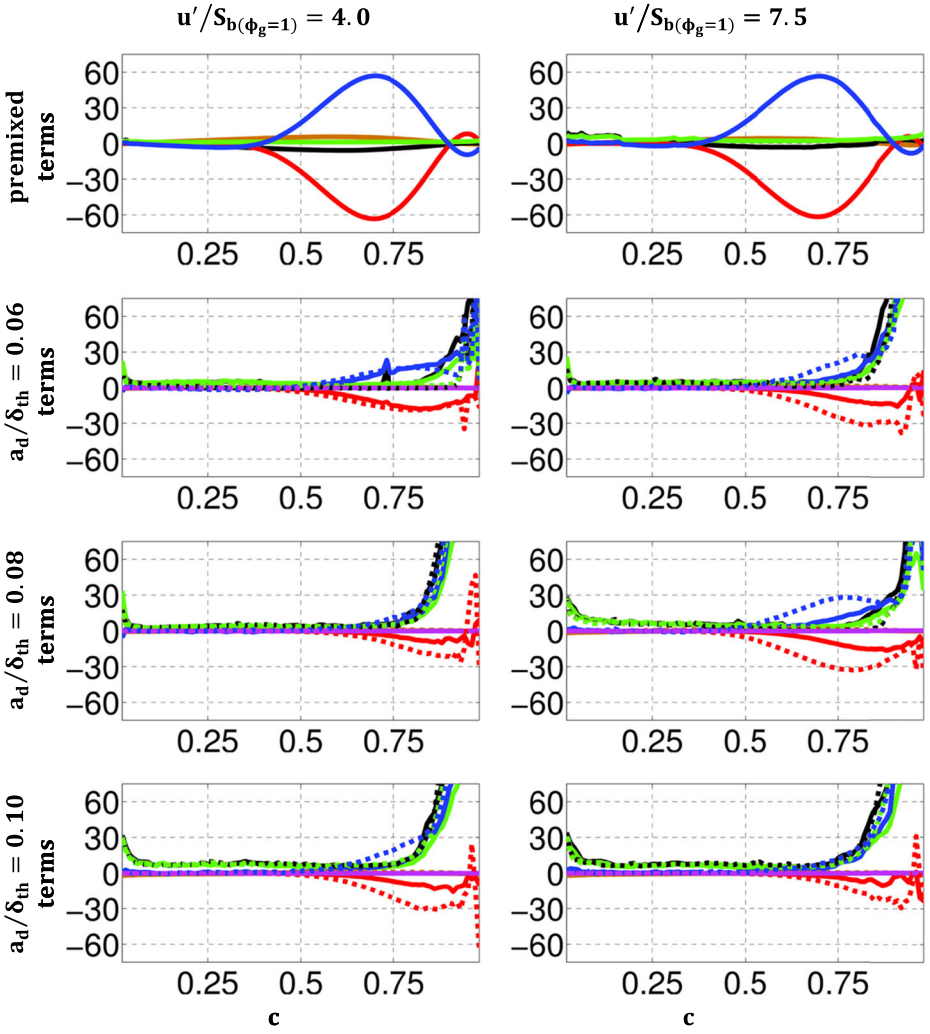

Fig. 8 Variation of conditional averages of flame-induced normal strain rate, $\langle N_j \partial S_d / \partial x_j \rangle_c$ (*black*), its components, $\langle N_j \partial S_i / \partial x_j \rangle_c$ where i = r, t, n, z (*red-green-blue-magenta*) and the normal strain rate a_N (*brown*) with c for (*top row*) stoichiometric premixed cases and (rows 2-4) droplet cases with $a_d / \delta_{th} = 0.06, 0.08, 0.10$ and $\phi_d = 1.00$ (*solid lines*) and 1.70 (*dashed lines*) under (*left to right columns*) turbulent flow conditions $u' / S_{b(\phi_g=1)} = 4.0, 7.5$. Terms have been normalised by $\delta_{th}/S_{b(\phi_g=1)}$. Component $\langle N_j \partial S_s / \partial x_j \rangle_c$ is not shown

whereas in the droplet cases both $\langle N_j \partial S_n / \partial x_j \rangle_c$ and $\langle N_j \partial S_t / \partial x_j \rangle_c$ remain predominantly positive and they significantly overcome the magnitude of the negative contribution of $\langle N_j \partial S_r / \partial x_j \rangle_c$. Thus the contributions of $\langle N_j \partial S_n / \partial x_j \rangle_c$ and $\langle N_j \partial S_t / \partial x_j \rangle_c$ tend to thicken the flame. Once again the magnitude of the contribution arising from normal diffusion component of displacement speed (i.e. $\langle N_j \partial S_n / \partial x_j \rangle_c$) is greater in the stoichiometric premixed cases than in the droplet cases. There is negligible difference in the contribution arising due to the tangential diffusion between $\phi_d = 1.00$ and 1.70, whereas the difference in the contribution arising due to the normal diffusion is non-negligible for some droplet sizes. For all droplet cases considered here, the contribution arising due to the normal and tangential diffusion components of $\langle N_j \partial S_d / \partial x_j \rangle_\xi$ remain positive for flammable mixtures (i.e. $0.03 < \xi < 0.09$), but the component arising due to reaction rate predominantly assumes negative values also in the mixture fraction space (not shown here).

The contribution of $\langle N_j \partial S_s / \partial x_j \rangle_c$ remains negligible for the major part of the flame and only assumes significant values towards the unburned gas side of the flame front where the evaporation takes place, especially for high turbulence intensity cases (e.g. initial $u' / S_{b(\phi_g=1)} = 7.5$ cases). A similar behaviour has been observed also in mixture fraction space and for this reason it is omitted from Fig. 8. The contribution of $\langle N_j \partial S_z / \partial x_j \rangle_\xi$ remains negligible in comparison to $\langle N_j \partial S_r / \partial x_j \rangle_\xi$, $\langle N_j \partial S_n / \partial x_j \rangle_\xi$, and $\langle N_j \partial S_t / \partial x_j \rangle_\xi$ and a similar behaviour has been observed in ξ space (not shown here) The net contribution of $\langle N_j \partial S_d / \partial x_j \rangle_c = \langle N_j \partial (S_r + S_n + S_t + S_z + S_s) / \partial X_j \rangle_c$ is positive in all cases and its magnitude significantly overcomes that of $\langle a_N \rangle_c$, especially for $c > 0.5$ and thus determines the behaviour of $\langle a_N + N_j \partial S_d / \partial x_j \rangle_c$, which assumes predominantly positive values and acts to thicken the flame. This is true for all droplet sizes and droplet equivalent ratios and for both turbulence intensities considered here. This in contrast to the stoichiometric premixed cases, in which the two most active components ($\langle N_j \partial S_r / \partial x_j \rangle_c$ and $\langle N_j \partial S_n / \partial x_j \rangle_c$) almost cancel out and the effective flame normal strain rate is governed by fluid-dynamic straining which has a much smaller magnitude than the strain rates induced by flame normal propagation due to displacement speed. Thus the flame thickness for turbulent premixed stoichiometric flames remains comparable to that of the unstrained laminar flame (e.g. the peak value of $\langle |\nabla c| \rangle \times \delta_{th}$ remains close to unity for turbulent stoichiometric premixed flames [19]).

The variation of $\langle a_T \rangle_c$ and $\langle 2 S_d \kappa_m \rangle_c$ and its components (i.e. $\langle 2 S_i \kappa_m \rangle_c$ where $i = r, t, n, z, s$) conditional on c for stoichiometric premixed flame cases and for droplet cases for $a_d / \delta_{th} = 0.06, 0.08, 0.10$ are shown in Fig. 9 for $\phi_d = 1.00$ and 1.70 in the case of turbulent flow conditions with initial $u' / S_{b(\phi_g=1)} = 4.0$ and 7.5. It can be seen from Fig. 9 that the contributions of $\langle 2 S_r \kappa_m \rangle_c$, $\langle 2 S_n \kappa_m \rangle_c$ and $\langle 2 S_t \kappa_m \rangle_c$ assume negative values and play dominant roles on the overall flame stretch rate in all droplet cases considered here and at both initial $u' / S_{b(\phi_g=1)} = 4.0$ and 7.5. However, in the case of the stoichiometric premixed flame this is true only for sufficiently high turbulence intensity (i.e. $u' / S_{b(\phi_g=1)} = 7.5$), in whose absence the above components assume negligible values. The contribution of the stretch rate induced by cross dissipation rate component of displacement speed $\langle 2 S_z \kappa_m \rangle_c$ remains negligible in comparison to the magnitude of negative values of $\langle 2 S_r \kappa_m \rangle_c$, $\langle 2 S_n \kappa_m \rangle_c$. A similar conclusion can also be drawn for the curvature stretch induced by the evaporation contribution of displacement speed $\langle 2 S_t \kappa_m \rangle_c$ but this contribution assumes non-negligible values towards the unburned gas side because of the relatively strong evaporation effects in that region although the contribution of $\langle 2 S_s \kappa_m \rangle_c$ remains negligible for the rest of the flame front.

For all droplet cases the components of $\langle 2 S_d \kappa_m \rangle_\xi$ arising due to reaction rate and normal and tangential diffusion components of displacement speed exhibit a strongly negative value

close to $\xi \approx \xi_{st}$, but for $\xi > \xi_{st}$ the $\langle 2S_r\kappa_m\rangle_\xi$ component exhibits positive values and acts in opposition to the negative values of $\langle 2S_n\kappa_m\rangle_\xi$ and $\langle 2S_t\kappa_m\rangle_\xi$ (not shown here).

The non-zero contributions of $\langle 2S_r\kappa_m\rangle_c$, $\langle 2S_n\kappa_m\rangle_c$ and $\langle 2S_t\kappa_m\rangle_c$ in statistically planar flames arise due to curvature κ_m dependence of displacement speed components S_r, S_n and S_t, which have been discussed in detail in Ref. [19]. These curvature dependences give rise to a complex non-linear curvature dependence of $\langle 2S_r\kappa_m\rangle_c$, $\langle 2S_n\kappa_m\rangle_c$, and $\langle 2S_t\kappa_m\rangle_c$ which gives rise to non-zero values of these terms. This behaviour can be substantiated from Fig.

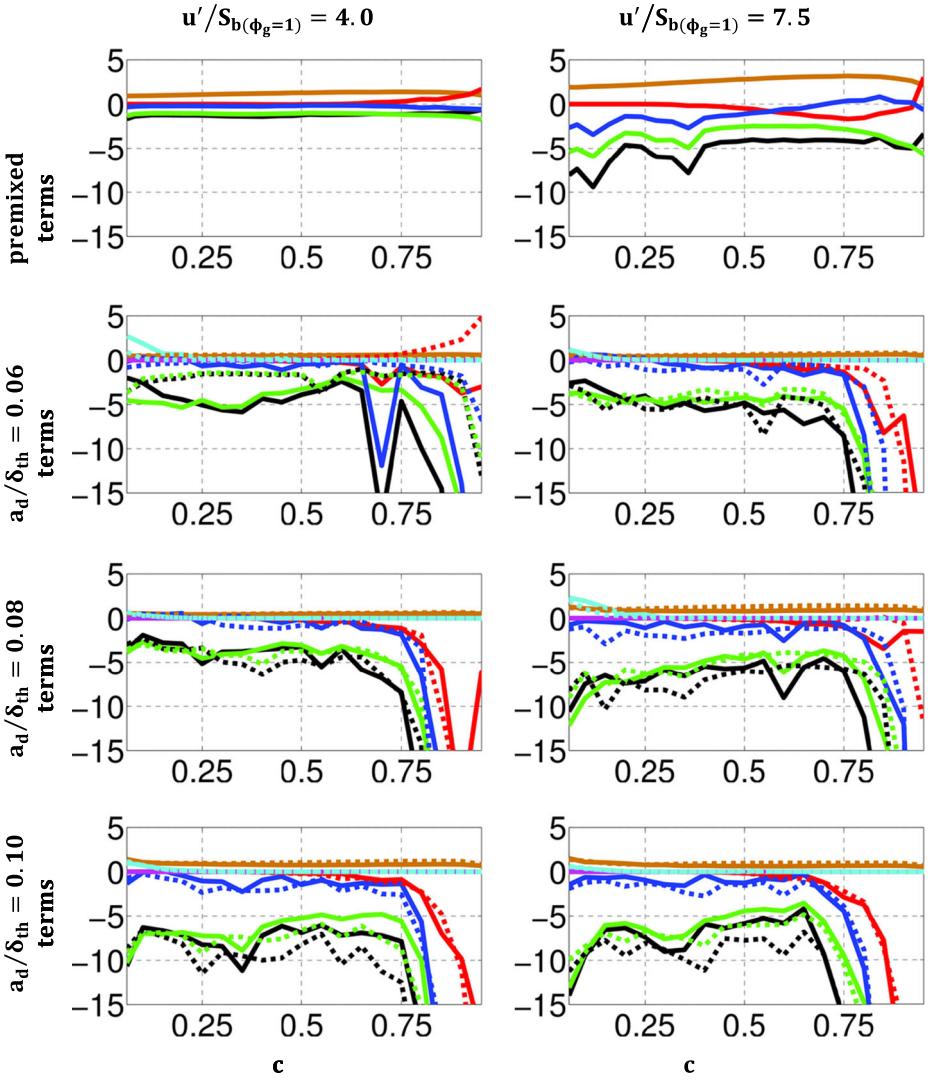

Fig. 9 Variation of conditional averages of curvature induced stretch, $\langle 2S_d\kappa_m\rangle_c$ (*black*), its components, $\langle 2S_i\kappa_m\rangle_c$ where i = r, t, n, z, s (*red-green-blue-magenta-cyan*) and the tangential strain rate a_T (*brown*) with c for (*top row*) stoichiometric premixed cases and (rows 2-4) droplet cases with $a_d/\delta_{th} = 0.06, 0.08, 0.10$ and $\phi_d = 1.00$ (*solid lines*) and 1.70 (*dashed lines*) under (*left to right columns*) turbulent flow conditions $u'/S_{b(\phi_g=1)} = 4.0, 7.5$. Terms have been normalised by $\delta_{th}/S_{b(\phi_g=1)}$

10 where the variation of averaged values of $2S_d\kappa_m$ (black solid line) and its components, $2S_i\kappa_m$ (where i = r, t, n, z, s) and the tangential strain rate a_T conditional on $\kappa_m \times \delta_{th}$ are shown for $0.50 < c < 0.90$ (where the effects of chemical reaction is significant [19]) in droplet cases with $a_d/\delta_{th} = 0.06, 0.08, 0.10$ and $\phi_d = 1.00$ and 1.70 under turbulent flow conditions with initial values of $u'/S_{b(\phi_g=1)} = 4.0$ and 7.5.

It can be seen from Figs. 9 and 10 that the magnitude of curvature stretch contribution $2S_d\kappa_m$ overcomes that of the tangential strain rate a_T, and thus the predominantly negative value of $2S_d\kappa_m$ leads to overall negative net stretch rate ($a_T + 2S_d\kappa_m$). The net negative

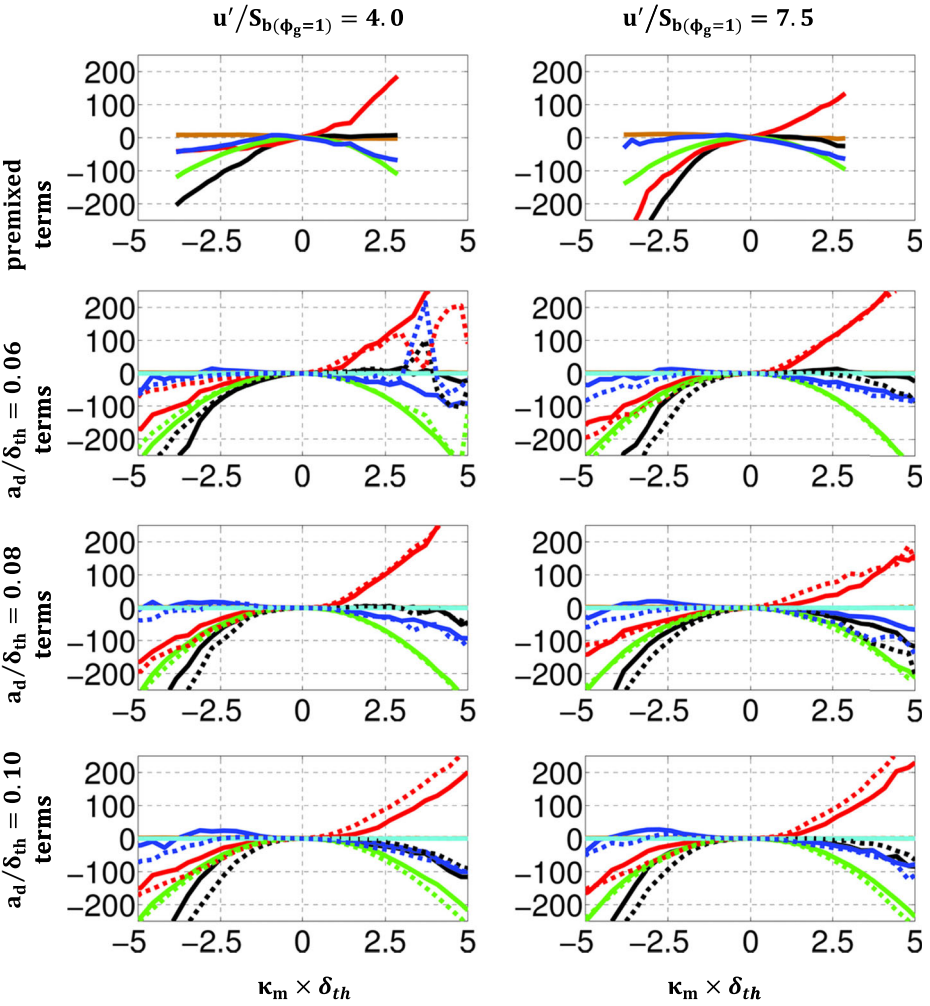

Fig. 10 Variation of ensemble-averaged values of curvature induced stretch, $2S_d\kappa_m$ (*black*), its components, $2S_i\kappa_m$ where i = r, t, n, z, s (*red-green-blue-magenta-cyan*) and the tangential strain rate a_T (*brown*) conditional on $\kappa_m \times \delta_{th}$ for $0.50 < c < 0.90$ for (*top row*) stoichiometric premixed and (rows 2-4) droplet cases with $a_d/\delta_{th} = 0.06, 0.08, 0.10$ and $\phi_d = 1.00$ (*solid lines*) and 1.70 (*dashed lines*) under (*left to right columns*) turbulent flow conditions $u'/S_{b(\phi_g=1)} = 4.0, 7.5$. Terms have been normalised by $\delta_{th}/S_{b(\phi_g=1)}$

stretch rate ($a_T + 2S_d\kappa_m$) also acts to reduce the flame surface area generation according to Eq. 27. Figure 9 suggests that the net stretch rate ($a_T+2S_d\kappa_m$) assumes negative values of higher magnitude in droplet cases than in the turbulent stoichiometric premixed flames under similar flow conditions and thus the flame area generation in droplet cases are expected to be smaller than in the corresponding turbulent stoichiometric premixed flames. This can indeed be verified from Fig. 4 of Ref. [19].

5 Conclusions

The effects of turbulence intensity, droplet diameter and droplet equivalence ratio on the statistical behaviour of the interaction of mono-disperse droplets with a statistically planar turbulent flames propagating into a droplet mist under decaying turbulence have been analysed based on three-dimensional modified one-step chemistry [32] DNS simulations. The fuel is supplied in the form of droplets in liquid phase which eventually evaporate and supply fuel in gaseous phase to support flame propagation. It has been found that the rms value of turbulent velocity u', initial droplet diameter a_d and droplet equivalence ratio ϕ_d have significant influences on the nature of the mixture arising due to droplet evaporation and that this is highly dependent on the position within the flame: $c < 0.9$ or $c > 0.9$. It was shown that although both premixed and non-premixed modes exist simultaneously in flames propagating into a droplet mist, but they reside predominantly in different locations in mixture fraction space: premixed mode in $\xi < \xi_{st}$ and non-premixed mode in $\xi \geq \xi_{st}$ A comparison with the flame thickness of a stoichiometric premixed flame by means of the SDF revealed that droplet laden mixtures exhibit thicker flames than the corresponding stoichiometric premixed flames. The flame thickening in droplet cases has been explained in terms of dilatation rate and strain rates induced by fluid motion and due to flame normal propagation arising from different components of displacement speed. The statistical behaviour of dilatation rate has been found to be affected by u', a_d and ϕ_d, and thus the thermal expansion effects in turbulent flame-droplet interaction are affected by the initial droplet diameter and droplet equivalence ratio ϕ_d. It was found that although the droplets predominantly evaporate in the preheat zone, however some droplets are able to penetrate the flame front. These droplets reach the burned gas side where they continue to evaporate such that some of the resulting fuel vapour diffuses back towards the flame front. The combustion process in gaseous phase takes place predominantly in fuel-lean mode even for $\phi_d > 1.0$. This leads to weakening of dilatation rate, flame straining and stretching due to reaction component of displacement speed in turbulent droplet cases in comparison to the corresponding turbulent stoichiometric premixed flames. The normal strain rate induced by fluid motion has been found to be significantly affected by turbulence intensity and droplet equivalence ratio because of their influences on turbulent straining and the strain induced by flame normal acceleration respectively, which in turn determine ∇c alignment with local principal strain rates and the statistical behaviour of fluid-dynamic normal strain rate. In all droplet cases the normal strain rate induced by the diffusion components of displacement speed assume predominantly positive values and they overwhelm the negative contribution arising from the reaction component of displacement speed and fluid dynamic straining. Thus, the effective normal strain rate in droplet cases assumes predominantly positive values and is principally governed by the diffusion components of displacement speed. By contrast, the normal strain rate contributions due to reaction and molecular diffusion components remain almost in equilibrium in stoichiometric premixed flames and thus the effective normal strain rate is principally determined by fluid dynamic straining. The predominant

positive values of effective strain rate are responsible for flame thickening in turbulent droplet cases in comparison to the corresponding stoichiometric premixed turbulent flames where the flame thickness remains comparable to that of the laminar unstrained premixed flame. The curvature dependence of displacement speed components yield complex non-linear curvature dependence of the curvature induced stretch rate which predominantly assumes negative values and overcomes positive contribution of positive tangential strain rate in droplet cases. By contrast, the net negative stretch rate in turbulent stoichiometric premixed flames has been observed due to high negative values of curvature induced stretch for high values of $u'/S_{b(\phi_g=1)}$ but the magnitude of this negative net stretch rate remains smaller than the droplet cases. The combination of higher probability of finding positive effective normal strain rate (i.e. combined contribution of fluid motion and flame propagation) and more negative values of stretch rate than in the stoichiometric premixed flame under similar flow conditions leads to thicker flame and smaller flame area generation in droplet cases. As the chemical mechanism has been simplified here by a modified one-step mechanism [32] for the purpose of computational economy, further analysis based on detailed chemistry will be necessary for deeper insight into the flame straining and stretching in flame-droplet interaction, which will form the basis of future analyses.

Acknowledgments The financial assistance of EPSRC (EP/J021997/1 and EP/K025163/1) and the computational resources of N8 and ARCHER are gratefully acknowledged. The authors are also grateful to Prof E. Mastorakos for his invaluable advice.

Compliance with ethical standards

Conflict of interests The authors declare that they have no conflict of interests

Research involving human participants and/or animals Not applicable for this paper.

Informed consent All the authors approve this submission.

References

1. Heywood, J.B. Internal Combustion Engine Fundamentals, 1st edn. McGraw Hills (1998)
2. Aggarwal, S.K.: A review of spray ignition phenomena: present status and future research. Prog. Energy Combust. Sci. **24**, 565–600 (1998)
3. Lefebvre, A.H. Gas Turbine Combustion, 2nd edn. Taylor & Francis, Ann Arbor, Michigan, USA (1998)
4. Bowen, P.: Combustion hazards posed by hybrid fuel systems. Proceedings 5th European Combustionis Meeting, Cardiff, UK (2011)
5. Burgoyne, J.H., Cohen, L.: The effect of drop size on flame propagation in liquid aerosols. Proc. Roy. Soc. Lond. A **225**, 375–392 (1954)
6. Szekely, Jr., G.A., Faeth, G.M.: Effects of envelope flames on drop gasification rates in turbulent diffusion flames. Combust. Flame **49**, 255–259 (1983)
7. Faeth, G.M.: Mixing, transport and combustion sprays. Prog. Energy Combust. Sci. **13**, 293–345 (1987)
8. Ballal, D.R., Lefebvre, A.H.: Flame propagation in heterogeneous mixtures of fuel droplets, fuel vapour and air. Proc. Combust. Inst. **18**, 312–328 (1981)
9. Hayashi, S., Kumagai, S., Sakai, T.: Propagation velocity and structure of flames in droplet-vapor-air mixtures. Combust. Sci. Technol. **15**, 169–177 (1976)

10. Silverman, I., Greenberg, J.B., Tambour, Y.: Stoichiometry and polydisperse effects in premixed spray flames. Combust. Flame **93**, 97–118 (1993)
11. Nomura, H., Koyama, M., Miyamoto, H., Ujiie, Y., Sato, J., Kono, M., Yoda, S.: Microgravity experiments of flame propagation in ethanol droplet-vapor-air mixture. Proc. Combust. Inst. **28**, 999–1005 (2000)
12. Aggarwal, S.K., Sirignano, W.A.: Unsteady spray flame propagation in a closed volume. Combust. Flame **62**, 69–84 (1985)
13. Lawes, M., Saat, A.: Burning rates of turbulent iso-octane aerosol mixtures in spherical flame explosions. Proc. Combust. Inst. **33**, 2047–2054 (2011)
14. Neophytou, A., Mastorakos, E.: Simulations of laminar flame propagation in droplet mists. Combust. Flame **156**, 1627–1640 (2009)
15. Nakamura, M., Akamatsu, F., Kurose, R., Katsuki, M.: Combustion mechanism of liquid fuel spray in a gaseous flame. Phys. Fluids **17**, 123301-123314 (2005)
16. Watanabe, H., Kurose, R., Hwang, S.-M., Akamatsu, F.: Characteristics of flamelets in spray flames formed in a laminar counterflow. Combust. Flame **148**, 234–248 (2007)
17. Watanabe, H., Kurose, R., Komori, S., Pitsch, H.: Effects of radiation on spray flame characteristics and soot formation. Combust. Flame **152**, 2–13 (2008)
18. Fujita, A., Watanabe, H., Kurose, R., Komori, S.: Two-dimensional direct numerical simulation of spray flames – Part 1: Effects of equivalence ratio, fuel droplet size and radiation, and validity of flamelet model. Fuel **104**, 515–525 (2013)
19. Wacks, D.H., Chakraborty, N., Mastorakos, E.: Statistical analysis of turbulent flame-droplet interaction: A Direct Numerical Simulation Study. Flow Turb. Combustion, doi:10.1007/s10494-015-9652-y (2015)
20. Miller, R.S., Bellan, J.: Direct numerical simulation of a confined three-dimensional gas mixing layer with one evaporating hydrocarbon-droplet-laden stream. J. Fluid Mech. **384**, 293–338 (1999)
21. Reveillon, J., Vervisch, L.: Spray vaporization in non-premixed turbulent combustion modelling: a single droplet model. Combust. Flame **121**, 75–90 (2000)
22. Wang, Y., Rutland, C.J.: Direct numerical simulation of ignition in turbulent n-heptane liquid-fuel spray jets. Combust. Flame **149**, 353–365 (2007)
23. Reveillon, J., Demoulin, F.X.: Evaporating droplets in turbulent reacting flows. Proc. Combust. Inst. **31**, 2319–2326 (2007)
24. Sreedhara, S., Huh, K.Y.: Conditional statistics of nonreacting and reacting sprays in turbulent flows by direct numerical simulation. Proc. Combust. Inst. **31**, 2335–2342 (2007)
25. Wandel, A., Chakraborty, N., Mastorakos, E.: Direct Numerical Simulation of turbulent flame expansion in fine sprays. Proc. Combust. Inst. **32**, 2283–2290 (2009)
26. Xia, J., Luo, K.H.: Direct Numerical Simulation of inert droplet effects on scalar dissipation rate in turbulent reacting and non-reacting shear layers. Flow. Turb. Combust. **84**, 397–422 (2010)
27. Neophytou, A., Mastorakos, E., Cant, R.S.: DNS Of spark ignition and edge flame propagation in turbulent droplet-laden mixing layers. Combust. Flame **157**, 1071–1087 (2010)
28. Luo, K., Pitsch, H., Pai, M.G., Desjardins, O.: Direct numerical simulations and analysis of three-dimensional n-heptane spray flames in a model swirl combustor. Proc. Combust. Inst. **33**, 2143–2152 (2011)
29. Wandel, A.: Influence of scalar dissipation on flame success in turbulent sprays with spark ignition. Combust. Flame **161**, 2579–2600 (2014)
30. Neophytou, A., Mastorakos, E., Cant, R.S.: Complex chemistry simulations of spark ignition in turbulent sprays. Proc. Combust. Inst. **33**, 2135–2142 (2011)
31. Neophytou, A., Mastorakos, E., Cant, R.S.: The internal structure of igniting turbulent sprays as revealed by complex chemistry DNS. Combust. Flame **159**, 641–664 (2012)
32. Tarrazo, E., Sanchez, A., Linan, A., Williams, F.A.: A simple one-step chemistry model for partially premixed hydrocarbon combustion. Combust. Flame **147**, 32–38 (2006)
33. Clift, R., Grace, J.R., Weber, M.E.: Bubbles, Drops and Particles. Academic Press, New York (1978)
34. Bray, K.N.C., Domingo, P., Vervisch, L.: Role of the progress variable in models for partially premixed turbulent combustion. Combust. Flame **431-437**, 141 (2005)
35. Malkeson, S.P., Chakraborty, N.: Statistical analysis of displacement speed in turbulent stratified flames: A Direct Numerical Simulation study. Combust. Sci. Technol. **182**, 1841–1883 (2010)
36. Candel, S.M., Poinsot, T.J.: Flame stretch and the balance equation for the flame area. Combust. Sci. Technol. **70**, 1–15 (1990)
37. Chakraborty, N., Cant, R.S.: Effects of strain rate and curvature on Surface Density Function transport in turbulent premixed flames in the thin reaction zones regime. Phys. Fluids **17**, 65108 (2005)

38. Dopazo, C., Cifuentes, L., Martin, J., Jimenez, C.: Strain rates normal to approaching iso-scalar surfaces in a turbulent premixed flame. Combustion Flame, doi:10.1016/j.combustflame.2014.11.034 (2014)
39. Jenkins, K.W., Cant, R.S.: DNS of turbulent flame kernels. In: Knight, D., Sakell, L. (eds.) Proceedings Second AFOSR Conference on DNS and LES, pp. 192–202. Rutgers University, Kluwer Academic Publishers (1999)
40. Wray, A.A.: Minimal Storage Time Advancement Schemes for Spectral Methods, Unpublished Report. NASA Ames Research Center, California (1990)
41. Poinsot, T.J., Lele, S.: Boundary conditions for direct simulations of compressible viscous flows. J. Comput. Phys. **101**, 104–129 (1992)
42. Rotexo-Softpredict-Cosilab, GmbH and Co. KG Bad Zwischenahn, Germany
43. Rogallo, R.S.: Numerical Experiments in Homogeneous Turbulence NASA Technical Memorandum, vol. 81315. NASA Ames Research Center, California (1981)
44. Grout, R.W.: An age-extended progress variable for conditioning reaction rates. Phys Fluids **105107**, 19 (2007)
45. Han, I., Huh, K.H.: Roles of displacement speed on evolution of flame surface density for different turbulent intensities and Lewis numbers in turbulent premixed combustion. Combust. Flame **152**, 194–205 (2008)
46. Reddy, H., Abraham, J.: Two-Dimensional Direct numerical simulation evaluation of the flame surface density model for flames developing from an ignition kernel in lean Methane/Air mixtures under engine conditions. Phys. Fluids **105108**, 24 (2012)
47. Pera, C., Chevillard, S., Reveillon, J.: Effects of residual burnt gas heterogeneity on early flame propagation and on cyclic variability in spark-ignited engines. Combust. Flame **160**, 1020–1032 (2013)
48. Peters, N.: Turbulent Combustion, Cambridge Monograph on Mechanics. Cambridge University Press, Cambridge (2000)
49. Yamashita, H., Shimada, M., Takeno, T.: A numerical study on flame stability at the transition point of jet diffusion flames. Proc. Combust. Inst. **26**, 27–34 (1996)
50. Chakraborty, N., Swaminathan, N.: Influence of the Damköhler number on turbulence-scalar interaction in premixed flames. I. Phys. Insight. Phys. Fluids **19**, 045103 (2007)
51. Hartung, G., Hult, J., Kaminski, C.F., Rogerson, J.W., Swaminathan, N.: Effect of heat release on turbulence and scalar-turbulence interaction in premixed combustion. Phys. fluids **20**, 035110 (2008)
52. Chakraborty, N., Klein, M., Swaminathan, N.: Effects of Lewis number on reactive scalar gradient alignment with local strain rate in turbulent premixed flames. Proc. Combust. Inst. **32**, 1409–1417 (2009)